Stellar mass loss from the Fornax dwarf spheroidal galaxy

Relatore:
Prof. Carlo Nipoti

Presentata da:
Marcello Cantari

Correlatore:
Dott. Giuliano Iorio
Dott. Francesco Calura

Contents

Sommario

Le galassie nane subiscono spesso interazioni gravitazionali da parte di compagne più massicce. Queste interazioni possono deformare le galassie, accendere o spegnere la formazione stellare o dar vita a fenomeni di perdita di massa. In questo lavoro di tesi ci proponiamo di studiare, tramite simulazioni N-body, la perdita di massa stellare subita dalla galassia nana sferoidale (dSph) Fornax in orbita attorno alla Milky Way. Un fenomeno chiave per spiegare il *mass budget problem*: gli ammassi globulari di Fornax possiedono, insieme, una massa stellare confrontabile con quella di Fornax stessa. Se osserviamo le popolazioni stellari di cui sono fatti e applichiamo gli scenari di formazione delle popolazioni stellari scopriamo che, in origine, dovevano essere almeno 5 volte più massicci. Quindi, devono aver perso o espulso stelle attraverso interazioni dinamiche. Tuttavia, come presentato in Larsen et al (2012), le sole stelle di campo non sono sufficienti per spiegare questo scenario. Possiamo assumere che parte di quelle stelle siano cadute in Fornax, e successivamente strappate dalla Milky Way. Per studiare questa soluzione abbiamo costruito diverse simulazioni illustrative, a singola componente, con un modello a densità tabulate, usando l'orbita P07ecc studiata da Battaglia et al (2015). Per dividere la singola componete in componente stellare e di materia oscura abbiamo definito una funzione di probabilità $\mathcal{P}(\mathcal{E})$ *a posteriori*, dove $\mathcal{E}$ è la distribuzione di energia iniziale delle particelle. Associando ad ogni particella una frazione di massa stellare e di materia oscura. In questo modo abbiamo costruito i profili di densità stellare senza ripetere simulazioni. Abbiamo applicato il metodo a Fornax usando le tabelle di densità dei profili ottenute da Pascale et al (2018) come vincoli osservativi e per costruire il modello. I risultati confermano i risultati precedentemente ottenuti con modelli meno flessibili in Battaglia et al (2015). Mostrano una perdita massa stellare $< 4\%$ all'interno dei 1.6 kpc e trascurabile nei 3 kpc, troppo piccola per risolvere il *mass budget problem*.

Abstract

Dwarf galaxies often experience gravitational interactions from more massive companions. These interactions can deform galaxies, turn star formation on or off, or give rise to mass loss phenomena. In this thesis work we propose to study, through N-body simulations, the stellar mass loss suffered by the dwarf spheroid galaxy (dSph) Fornax orbiting in the Milky Way gravitational potential. Which is a key phenomenon to explain the *mass budget problem*: the Fornax globular clusters together have a stellar mass comparable to that of Fornax itself. If we look at the stellar populations which they are made of and we apply the scenarios of stellar population formation we find that, originally, they must have been $\geq$ 5 times more massive. For this reason, they must have lost or ejected stars through dynamic interactions. However, as presented in Larsen et al (2012), field stars alone are not sufficient to explain this scenario. We may assume that some of those stars fell into Fornax, and later were stripped by Milky Way. In order to study this solution we built several illustrative single component simulations, with a tabulated density model using the P07ecc orbit studied from Battaglia et al (2015). To divide the single component into stellar and dark matter components we have defined *a posterior* the probability function $\mathcal{P}(\mathcal{E})$, where $\mathcal{E}$ is the initial energy distribution of the particles. By associating each particle with a fraction of stellar mass and dark matter. In this way we built stellar density profiles without repeating simulations. We applied the method to Fornax using the profile density tables obtained in Pascale et al (2018) as observational constraints and to build the model. The results confirm the results previously obtained with less flexible models by Battaglia et al (2015). They show a stellar mass loss $< 4\%$ within 1.6 kpc and negligible within 3 kpc, too small to solve the *mass budget problem*.

Chapter 1

Introduction

The current favoured cosmological model, the ΛCDM, describes a flat geometry universe ($\Omega_0 + \Omega_{\Lambda 0} = 1$) where the contribution is given to $\sim 70\%$ by dark energy and $\sim 30\%$ by matter. Of this mass $\sim 85\%$ is due to dark matter while $\sim 15\%$ is due to baryonic matter (42).

Within the ΛCDM model, the formation of massive galaxies and larger structures such as groups and clusters occurs by merging of smaller objects, such as dwarf galaxies. This scenario is defined as hierarchical or bottom-up.

These small objects are formed from a halo of dark matter ($M_{\mathrm{gal}} > 10^6$ M$_\odot$) in which baryonic matter collapse, cools and form stars. These first stars are born in an environment of zero metallicity (8). When they die they can either explode as supernovae, causing the release of an enormous quantity of energy in the primordial gas, or they can collapse directly into a black hole (19). The primordial gas, invested by this energy in the form of shock waves, is swept away.

By that time, these young dark matter halos must have masses $\geq 10^8$ M$_\odot$ (9) to gravitationally retain this gas. Otherwise, the gas is ejected into intergalactic space, the star formation stops and we get an empty dark matter halo without optical counterpart.

An objects that can withstand this scenario will then evolve into proto-dwarf galaxy or dwarf galaxy (17).

We can define galaxies as self-gravitating objects in equilibrium, capable of gravitationally retaining a substantial fraction of the gas to prolong star formation (9). They have total masses between 10^8 M$_\odot$ and 10^{13} M$_\odot$, size of $1 - 200$ kpc and their luminosity distribution is generally well described by the Schechter function (41). They show different morphologies related to environmental characteristics (15) and their history of star formation

or merging history (43).

Historically, the earliest classifications of galaxies, such as the Hubble tuning fork, were based on their morphological type. However, today there are more complex classifications based on single physical parameters.

The one of our interest, and which is discussed in section 1.1, is the classification of dwarf galaxies.

1.1 Properties of dwarf galaxies.

Dwarf galaxies exhibit a wide variety of shapes and physical characteristics due to their low mass, which makes them easily influenced by more massive objects and their own star formation (33).

These influences can be tidal forces (37) or ram pressure and can strip dark matter from the halo and baryonic matter in the form of stars and gas. This phenomenon can be so violent or protracted over time that can leave the galaxy without a dark matter halo (30). Without a sufficient quantity of gas, and the possibility of accreting it through infall or mergers, it is difficult to have an extended star formation with multiple stellar populations, it is easier to find simple stellar populations born from burst events. Such a star formation history can explain the low surface brightness of these objects and their high mass-to-light ratios (17).

Choosing an unambiguous definition of a dwarf galaxy is generally difficult; one possible choice is to take as a threshold a certain magnitude ($M_V \geq -18$ mag) beyond which a galaxy is considered a dwarf. For this reason they are not easy to observe and the best-known ones belong to the Local Group (32), (44). The most general classification we can make for these objects is between irregular, spherical and spheroidal dwarf galaxies (18).

- (dIrr) Dwarf irregular ($M_V \geq -18$ mag, $M_{\mathrm{DM+star}} \leq 10^{10}$ M$_\odot$) are rich in gas, far from massive objects (fig 1.1), they have rotational support, show the presence of recent star formation, and typical metallicity 0.1 Z$_\odot$.

- (dEs) Dwarf spherical ($M_V \geq -17$ mag, $M_{\mathrm{DM+star}} \leq 10^{9}$ M$_\odot$) are globular cluster-like objects with a pronounced central concentration; all the dEs of the Local Group are companions of M31.

- (dSph) Dwarf spheroidal ($M_V \geq -14$ mag, $M_{\mathrm{DM+star}} \sim 10^{7}$ M$_\odot$) are almost without gas, with multiple stellar populations and the stars are generally old-intermediate age. They are not supported by rotation and show the highest mass-to-light ratios ($M/L > 10$). They also show signs of segregation in their spatial distribution in the Local Group (see fig 1.1).

Another important factor for these galaxies is the presence or absence of globular clusters which, due to low masses, can have a decisive impact on their evolutionary history. In particular, Fornax is the dSph with the

highest number of globular cluster in the Local Group. Several studies exploit this peculiarity to find constrains on the evolution of this type of systems (39) or Fornax itself (10) (6) (22).
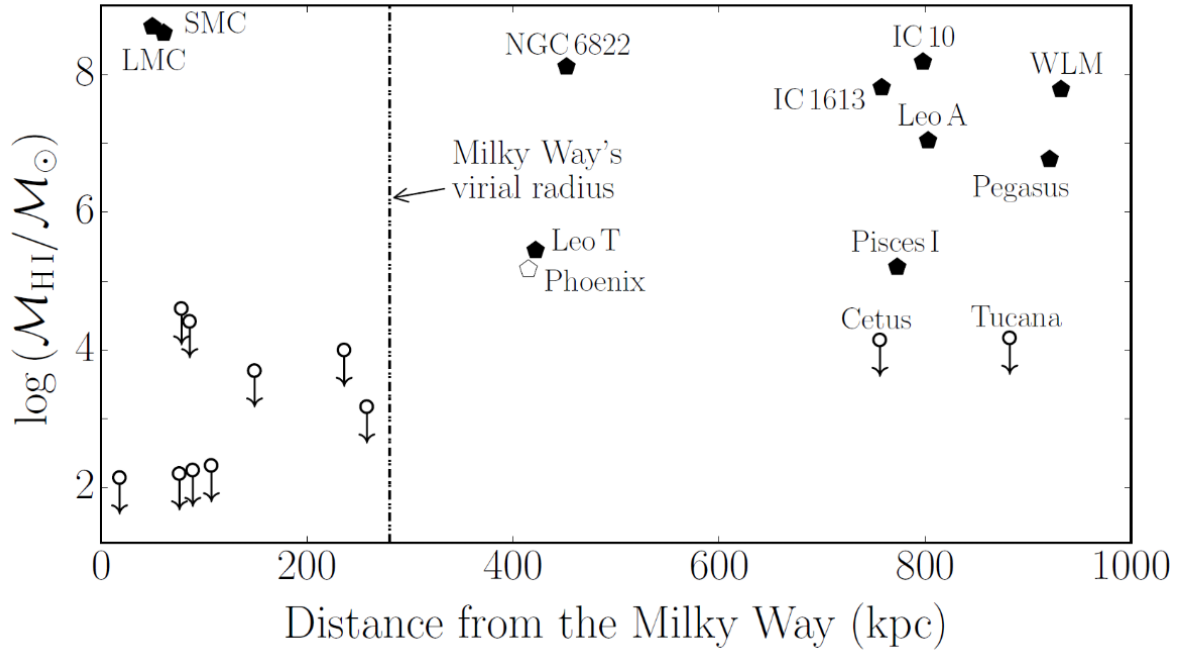

Figure 1.1: The HI gas content of dwarf galaxies as a function of their Galactocentric distance. Arrows are upper limits and are where essentially no gas is detected. This figure is taken from (9).

1.2 Fornax's Mass budget problem

Fornax is a dwarf galaxy classified as dSph. It is located at 138 ± 8 kpc from us (13), in the coordinate position shown in tab 1.1 (3), it is the second dSph for brightness ($M_V = -13.2$ mag) (31) and for mass ($M_{\text{tot}} \sim 10^9$ M$_\odot$) within the Local Group and shows a complex and articulated star formation history, which continued until 100 Myr ago (11).

Within Fornax, we can identify three different stellar populations (40):

- Old population (> 10 Gyr): the old population is made up of stars with metallicity of $-2.2 < [Fe/H] < -1.4$. It is distributed in the volume of the galaxy.

- Intermediate population ($2 - 10$ Gyr): the intermediate population formed over a wide time, with were at least two peaks of star formation 7 and 2.5 Gyr ago. With a metallicity of $-1.25 < [Fe/H] < -0.75$, this population is dominant in the centre of the galaxy.

- Young population (< 1 Gyr): it mainly formed in a star formation episode of 100 Myr ago, it has metallicity of $[Fe/H] \sim -0.7$ and it is mainly segregated in the center.

In addition to these stellar populations, Fornax has five globular clusters. We define the specific frequency parameter as:

$$S_{\text{N}} = N_{\text{GC}} 10^{0.4 \cdot (M_V + 15)} \qquad (16) \qquad\qquad (1.1)$$

which is the number of globular cluster per unit luminosity, normalized at 15 mag. For Fornax we obtain $S_{\text{N}} = 26$ (26), is a large number for a galaxy with Fornax characteristics, since a normal quantity does not go beyond 20. Typically, spirals, ellipticals and cD galaxies have $S_{\text{N}} \sim 1$, $3 - 5$ and $10 - 20$, respectively (16).

The value increases even more if we consider only the stars with a metallicity of $[Fe/H] < -2$. This is because four out of Fornax's five globular clusters present old stars with metallicity $[Fe/H] < -2$ (Fornax 1, 2, 3, 5 (25) (27)). In these conditions $M_V([Fe/H] < -2) \sim -10$ mag and $S_{\text{N}}([Fe/H] < -2) \approx 400$ (26). If we compare Fornax's stellar mass ($M_{\star,\text{Fornax}} \approx 4.3 \cdot 10^7$ M$_\odot$ (13)) with the total stellar mass of its globular clusters, we find that they are comparable, i.e. $M_{\star,\text{tot,GC}} \approx 10^6$ M$_\odot$ (14). Within the globular clusters of Fornax we find multiple stellar populations (27). In particular, there are first generation stars (1G) and second

generation stars (2G) which show anti-correlations in the abundances of different elements, such as O-Na or C-Na.

Scenarios for the formation of multiple populations (23) predict that the first generation enriches the gas and, together with an amount of gas accreted from the surrounding environment, it enables the formation of a second generation. However, for a standard IMF (24), only a low percentage of this enriched gas can be used to create the next generation. This led to he so-called *mass-buget problem*; a solution to this problem is to assume either a non-standard IMF for 1G stars, or postulate a 1G more massive than the present-day GCs by a factor between 5-20 (38). However, Fornax field stars have in total a stellar mass equal to, at most, 4-5 times of the present globular clusters mass (26). This implies that, in order to justify very large FG mass values ($\gg 5$), we are forced to require that a large fraction (90 - 95%) of 1G stars was somehow lost after enriching the gas.

An intuitive solution may be to call into question the tidal forces suffered by Fornax and their contribution to its evolutionary history. A loss of stellar mass can explain such a high specific frequency and low total stellar mass in Larsen's field stars. Based on where they were lost, and when, these stars may no longer be detectable. This possibility was already investigated (4) with less flexible models.

What we intend to do in this thesis is to study, through N-body simulations, the loss of stellar mass suffered by a Fornax-like satellite. We take advantage from previous work to put constraints on Fornax mass density distribution from Pascale et al (2018)(36) and orbital parameters from Battaglia et al (2015) (4).

Parameter	Value
RA	$2^h 39^m 52^s$
DEC	$-34°30'49''$
P.A.	$46°.8 \pm 1°.6$
ϵ	0.30 ± 0.01
$v_{\mathrm{sys,h}}$	54.1 ± 0.5 km/s

Table 1.1: Observational parameters of Fornax: right ascension (RA), declination (DEC), Position Angle (P.A.), ellipticity (ϵ). P.A. is the angle between the North and the projected major axis of the galaxy measured anti-clockwise. $v_{\mathrm{sys,h}}$ refers to the heliocentric reference frame. The table is from (2).

Chapter 2

Main proprieties of collisionless systems

In this chapter we discuss the main properties of collionless stellar system following the treatment of (7).

By non-collisional system we mean a system that has an age lower than its two-body relaxation time.

In this type of systems, such as galaxies, the interactions between stars are irrelevant because their motion is dominated by the smooth gravitational potential. The gravitational interactions between individual stars are negligible and retain the motions dating back to their formation. Furthermore, a collisionless system is not automatically in equilibrium. The condition of relaxation, on the other hand, is achieved through a redistribution of energy between all parts of the system with collisions, bringing the system to equilibrium.

There are two methods of doing this: through collision between particles (two-body relaxation time) or through variations of the gravitational potential (violent relaxation time). Of these two phenomena, the longest is the two-body relaxation time, beyond which we are sure that the system is relaxed.

To understand how the collisions between the stars can lead the system to a redistribution of energy we must study how these exchanges of energy take place.

2.1 Two body relaxation time

For the demonstration of the two-body relaxation time we consider a system (fig 2.1) with two particles, one at rest (p1, black dot) and one moving along a trajectory x (p2). We define v_{ini} as the initial velocity of the p2 particles and $\delta v_\perp$ as the variation in velocity perpendicular to the straight line trajectory. Then, we can consider the trajectory of a particle to be significantly deviated if $\delta v_\perp \sim v_{\text{ini}}$.
For the demonstration we use *impulse approximation*, we put ourselves in the center of reference of p1, we approximate the orbit of the deviated body with a straight line (dashed line), at speed $v = cost$, at distance $b = cost$ from p1, fig 2.1. This is what we define collision: in terms of the parametr b we can then talk about a close encounter ($\approx b_{\text{min}}$) or a far encounter ($\approx b_{\text{max}}$).
The $F_\perp$ is the force perpendicular to the trajectory of the 2p particle. We can calculate it as:

$$F_\perp = -\frac{Gm^2}{x^2 + b^2}\cos\theta = -\frac{Gm^2}{x^2 + b^2}\frac{b}{(x^2 + b^2)^{1/2}} \; , \qquad (2.1)$$

the corresponding deviation is:

$$\delta v_\perp = \frac{1}{m}\int_{-\infty}^{\infty} F_\perp \mathrm{d}t = -Gm^2 b \int_{-\infty}^{\infty} \frac{1}{(x^2 + b^2)^{3/2}}\mathrm{d}t = -\frac{2Gm}{bv} \qquad (2.2)$$

we choose to make a substitution, taking into account that $x = vt$, with $\tilde{x} = \frac{x}{b}$ we can change $\int \mathrm{d}t \to \int \mathrm{d}\tilde{x}$ and we obtain:

$$\delta v_\perp = -\frac{2Gm}{bv} \quad . \qquad (2.3)$$

If we take into account all the deviations that the particle undergoes while crossing the system at a distance between b and $b + \mathrm{d}b$ we obtain: $\frac{N}{\pi R^2}2\pi b\mathrm{d}b$, where N is the total number of particles and R is the radius. We assume that all these variations occur randomly, with this condition the average deviation of the particle will follow a Gaussian centered at 0, $\delta v_\perp = 0$. But, its perpendicular kinetic energy changes at every deviation:

$$\langle \Delta v^2 \rangle (b) \approx (\delta v)^2 \frac{2N}{R^2} b\mathrm{d}b \quad . \qquad (2.4)$$

We integrate across the entire range of impact parameters:

$$\langle \Delta v^2 \rangle = \frac{8G^2 m^2 N}{v^2 r^2}\int_{-b_{\text{min}}}^{b_{\text{max}}} \frac{\mathrm{d}b}{b} = 8N\left(\frac{Gm}{Rv}\right)^2 \ln\Lambda \quad , \quad \Lambda = \frac{b_{\text{max}}}{b_{\text{min}}} \qquad (2.5)$$

where the value of $b_{\min}$ is obtained from our definition of significant deviation, such that $v \approx \delta v = \frac{Gm}{b_{\min}v}$. The value of $b_{\max}$ instead is given by the size of the system, $b_{\max} = R$, so

$$\Lambda = \frac{b_{\max}}{b_{\min}} = \frac{R}{Gm}\frac{v^2}{2} = \frac{N}{v_c^2}\frac{v^2}{2} \approx \frac{N}{2} \approx N \ . \tag{2.6}$$

With a ratio $n_{\text{relax}} \approx \frac{v^2}{\langle \Delta v^2 \rangle}$ we find the number of steps that the particle must go through to have an energy $\Delta K \sim K$:

$$n_{\text{relax}} = \frac{v^4}{N}\frac{R^2}{G^2m^2}\frac{1}{8\ln\Lambda} \approx \frac{N}{8\ln\Lambda} \approx \frac{N}{8\ln N} \tag{2.7}$$

Multiplying by the characteristic time of a passage, $t_{\text{cross}} = \frac{2\pi R}{v}$ we find the two-body relaxation time:

$$t_{\text{2B-relax}} = n_{\text{relax}}t_{\text{cross}} \approx \frac{N}{8\ln N}t_{\text{dyn}} \ , \tag{2.8}$$

where t_{dyn} is calculated as:

$$t_{\text{dyn}} = \frac{1}{\sqrt{G\bar{\rho}}} = \sqrt{\frac{8\frac{4}{3}\pi r_{\text{half mass}}^3}{GM}} = \sqrt{\frac{32\pi}{3}}\sqrt{\frac{r_{\text{half mass}}^3}{M}} \quad . \tag{2.9}$$

The time found in 2.8 is the two-body relaxation time. It measures how long it takes the system to redistribute energy through only collisions. For a Milky Way-like galaxy with $N \approx 10^{11}$ we find $t_{\text{2B-relax}} = 10^{6-7}$ Gyr. For a dwarf galaxy, with $N \approx 10^7$, $t_{\text{2B-relax}} = 10^{11}$ Gyr.
Galaxies therefore cannot be systems that have achieved relaxation through collisions. Ideally, with infinite time, all systems relax through collisions and go from non-collisional to collisional. However the galaxies are too young compared to their relaxation time, so they must have relaxed otherwise.
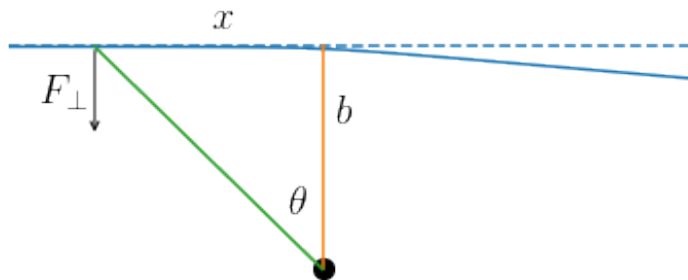
Figure 2.1: Two-particle system.

2.2   Violent relaxation time

Another mechanism to relax the system was proposed in 1967 by Lynden (29). It is the violent relaxation, a chaotic and collective process that can only be studied through simulations. While the two-body relaxation redistributes the energies by changing the speed of the particles to have particles with similar energy, the violent relaxation changes the energy of the particles by uniforming their speed.

Violent relaxation is possible as long as the gas present for star formation, or any other element that can allow energy to be dissipated, is exhausted. Under these conditions it is possible to distribute the energy with the variation of the gravitational potential.

We define the energy of a single star orbiting in a time-varying gravitational potential $\Phi(\mathbf{r}, t)$ as:

$$E(\mathbf{v}, t) = \frac{v^2}{2} + \Phi(\mathbf{r}, t) \quad . \tag{2.10}$$

The variation of the star's energy over time is given by:

$$\frac{dE}{dt} = \frac{\partial E}{\partial \mathbf{v}} \cdot \frac{d\mathbf{v}}{dt} + \frac{d\Phi}{dt} = -\mathbf{v} \cdot \nabla\Phi + \frac{\partial \Phi}{\partial \mathbf{r}} \cdot \frac{d\mathbf{r}}{dt} + \frac{\partial \Phi}{\partial t} = \frac{\partial \Phi}{\partial t} \tag{2.11}$$

and this will happen with a characteristic time of:

$$t_{\text{V-relax}} = \left\langle \frac{\dot{E}^2}{E^2} \right\rangle^{-1/2} = \left\langle \frac{\dot{\Phi}^2}{E^2} \right\rangle^{-1/2} = \frac{3}{4} \cdot \left\langle \frac{\dot{\Phi}^2}{\Phi^2} \right\rangle^{-1/2} \approx t_{\text{cross}} \quad . \tag{2.12}$$

Violent relaxation is a faster process that allows the system to become relaxed in a few dynamical time.

$$t_{\text{V-relax}} \approx t_{\text{cross}} \approx t_{\text{dyn}} \ll t_{\text{2B-relax}} \tag{2.13}$$

Ideally this process requires an infinite mass to reach its fulfillment, only the central regions of the object are in equilibrium while in the outer parts we expect anisotropies.

2.3 Collisionless Boltzmann Equation (CBE)

In this, and the next section, we introduce the theoretical framework that we will use to generate positions and velocities of the particles of the Fornax-like satellite.
We define the distribution function (DF hereafter) as the function f such that:

$$f(\mathbf{w}, t)\mathrm{d}^6\mathbf{w} \ , \tag{2.14}$$

with $\mathbf{w} = (\mathbf{x}, \mathbf{v})$ is the number of stars in an infinitesimal phase-space volume $\mathrm{d}^6\mathbf{w}$ centered in $\mathbf{w}$ at time t.
We define the integral of the distribution function as

$$\int f(\mathbf{w}, t)\mathrm{d}^6\mathbf{w} = \mathrm{N} \tag{2.15}$$

The DF contains all the information about the system. To obtain them we need to study the moments of the distribution of the DF.
The study of the first moments are

$$\text{Number density} \quad n(\mathbf{x}) = \int f(\mathbf{x}, \mathbf{v}, t)\mathrm{d}^3\mathbf{v} \tag{2.16}$$

$$\text{Mean velocity} \quad \overline{v} = \frac{1}{n(\mathbf{x})} \int v f(\mathbf{x}, \mathbf{v}, t)\mathrm{d}^3\mathbf{v} \tag{2.17}$$

We can easily arrive at the total mass of the system, or the mass density, by considering m as the mass of a single star and multiplying it by 2.15.
What interests us most is to determine the f. If what we need is a non-collisional system then we require that the probability of finding a particle in one position does not affect the probability of finding a particle

in another position.

As result, the distribution function must be such that:

$$f^N(\mathbf{w}_1, \mathbf{w}_2, \ldots, \mathbf{w}_N, t) = \prod_{i=1}^{N} f(\mathbf{w}_i, t) \tag{2.18}$$

Since the space inside a galaxy is mostly empty, the direct collisions between stars are highly unlikely, we can consider the stars as a fluid whose mass its conserved:

$$\frac{\partial f}{\partial t} + \sum_{i=1}^{6} \frac{\partial (f \dot{w}_i)}{\partial w_i} = 0 \;, \tag{2.19}$$

which gives

$$\begin{aligned}
\sum_{i=1}^{6} \frac{\partial (f \dot{w}_i)}{\partial w_i} &= \sum_{i=1}^{6} \frac{\partial (\dot{w}_i)}{\partial w_i} f + \sum_{i=1}^{6} \dot{w}_i \frac{\partial (f)}{\partial w_i} \\
&= \sum_{j=1}^{3} \frac{\partial v_j}{\partial x_j} - \sum_{j=1}^{3} \frac{\partial}{\partial v_j} \frac{\partial \Phi}{\partial x_j} + \sum_{i=1}^{6} \dot{w}_i \frac{\partial (f)}{\partial w_i} \;,
\end{aligned} \tag{2.20}$$

where the two canceled terms are eliminated because x_j and v_i are independent coordinates and $\frac{\partial \Phi}{\partial x_i} = \dot{v}_j$.

This is the Collisionless Boltzmann Equation (CBE hereafter):

$$\frac{\partial f}{\partial t} + \sum_{i=1}^{6} \dot{w}_i \frac{\partial f}{\partial w_i} = 0 \;, \tag{2.21}$$

or

$$\frac{\partial f}{\partial t} + v_i \frac{\partial f}{\partial x_i} - \frac{\partial \Phi}{\partial x_i} \frac{\partial f}{\partial v_i} = 0 \;. \tag{2.22}$$

2.3.1   Jeans Equation

Jeans equations are an infinite series of equations obtainable from CBE by a function of v and integrated over velocities.

In this way the problem goes from finding a solution for the CBE to being able to close the infinite series of Jeans' equations, where each equation gives information about the physical quantities of the system.

In order to obtain the Jeans equation we combine eq 2.22, 2.16 and 2.17 to write the continuity equation:

$$\int (\text{CBE}) \mathrm{d}^3\mathbf{v} = \frac{\partial}{\partial t} \int f \mathrm{d}^3\mathbf{v} + \frac{\partial}{\partial x_i} \int v_i f \mathrm{d}^3\mathbf{v} - \frac{\partial \Phi}{\partial x_i} \int \frac{\partial f}{\partial v_i} \mathrm{d}^3\mathbf{v}$$

$$= \frac{\partial n(\mathbf{x})}{\partial t} + \frac{\partial n\overline{v_i}}{\partial x_i} - \frac{\partial \Phi}{\partial x_i} \int \mathrm{d}v_j \int \mathrm{d}v_k \cancel{\int \frac{\partial f}{\partial v_i} \mathrm{d}v_i} \qquad (2.23)$$

$$= \frac{\partial n}{\partial t} + \frac{\partial n\overline{v_i}}{\partial x_i} = 0 \ .$$

The second Jeans equation is:

$$\int (\text{CBE}) v_j \mathrm{d}^3\mathbf{v} = \frac{\partial}{\partial t} \int v_j f \mathrm{d}^3\mathbf{v} + \frac{\partial}{\partial x_i} \int v_i v_j f \mathrm{d}^3\mathbf{v} - \frac{\partial \Phi}{\partial x_i} \int \frac{\partial f}{\partial v_i} v_j \mathrm{d}^3\mathbf{v}$$

$$= \frac{\partial n\overline{v_i}}{\partial x_j} + \frac{\partial n\overline{v_i v_j}}{\partial x_j} - \frac{\partial \Phi}{\partial x_i} \left(\cancel{\int \frac{\partial (f v_j)}{\partial v_i}} - \int \frac{\partial v_j}{\partial v_i} f \right) \mathrm{d}^3\mathbf{v}$$

$$= \frac{\partial n}{\partial t} + \frac{\partial n\overline{v_i}}{\partial x_i} + n\frac{\partial \Phi}{\partial x_j} = 0 \ .$$

$$(2.24)$$

We can rewrite this second equation in a more useful form by considering the velocity dispersion tensor, defined as:

$$\sigma_{ij}^2 = \overline{(v_i - \overline{v_i})(v_j - \overline{v_j})} = \frac{1}{n} \int f(v_i - \overline{v_i})(v_j - \overline{v_j}) \mathrm{d}^3\mathbf{v} \ . \qquad (2.25)$$

The second Jeans equation becomes:

$$n\frac{\partial \overline{v_j}}{\partial t} + \frac{\partial (n\sigma_{ij}^2)}{\partial x_i} + n\overline{v_i}\frac{\partial \overline{v_j}}{\partial x_i} + n\frac{\partial \Phi}{\partial x_j} = 0 \ . \qquad (2.26)$$

2.4   Jeans theorem

The integrals of motion are defined as functions $I(\mathbf{x}, \mathbf{v})$ such that:

$$\frac{\mathrm{d}I}{\mathrm{d}t} = \frac{\partial I}{\partial \mathbf{x}} \frac{\mathrm{d}\mathbf{x}}{\mathrm{d}t} + \frac{\partial I}{\partial \mathbf{v}} \frac{\mathrm{d}\mathbf{v}}{\mathrm{d}t} = \mathbf{v}\frac{\partial I}{\partial \mathbf{x}} - \frac{\partial \Phi}{\partial \mathbf{x}} \frac{\partial I}{\partial \mathbf{v}} = 0 \ . \qquad (2.27)$$

The 2.27 equation it's like 2.22 with $\frac{\partial}{\partial t} = 0$ (also known as equilibrium collisionless Boltzmann equation, eCBE hereafter). So, the integrals of motion are stationary solutions for the CBE.

Jeans theorem 2.4.1 *Any function of the integrals of motion is a solution of the eCBE. Furthermore, any solution of the equilibrium collisionless Boltzmann equation only depends on the phase-space coordinates $(\mathbf{x}, \mathbf{v})$ through the integrals of motion. (7)*

Therefore, if we have some integrals of motion $I_1, \ldots, I_n$ every DF like $f = f(I_1), f(I_1, I_2), \ldots, f(I_1, \ldots, I_n)$ is a CBE solution.

The Jeans theorem implies that if we are looking for solutions for the stationary CBE, we must look for a function that depends on prime integrals of motion and that is positive for all values of $(\mathbf{x}, \mathbf{v})$ (7). This for example allows us to build a galaxy orbit by orbit.

For the spherical systems the possible candidates are the energy E and the angular momentum $\mathbf{L}$. We choose to consider only DF energy dependent $f(E)$, which are known as ergodic DF.

2.5 Ergodic DF for sperical system

The simplest CBE solution, for a self-consistent system, is a DF that depends only on energy. By self-consistent we indicate a system in which density determines potential and potential determines density consistently via the Poisson equation.

In order to determine our $f(E)$ we define:

$$\text{Relative Potential} \quad \Psi = -\Phi + \Phi_0 \ , \tag{2.28}$$

$$\text{Relative Energy} \quad \mathcal{E} = -E + \Phi_0 = \Psi - \frac{1}{2}v^2 \ , \tag{2.29}$$

where Φ_0 is defined such that $f > 0$ if $\mathcal{E} > 0$ and $f = 0$ if $\mathcal{E} \leq 0$.

Then, the Poisson equation in terms of the relative potential is

$$\nabla^2 \Psi = -4\pi G \rho \ . \tag{2.30}$$

We rewrite the density with eq 2.29

$$\rho(r) = \int d\mathbf{v} f(r, \mathbf{v})$$

$$= 4\pi \int f(r, v) dv$$

$$= 4\pi \int v^2 f(\mathcal{E}) dv \tag{2.31}$$

$$= 4\pi \int_0^\Psi \sqrt{2(\Psi - \mathcal{E})} f(\mathcal{E}) d\mathcal{E}$$

$$\frac{1}{\sqrt{8}\pi} \rho(\Psi) = 2 \int_0^\Psi \sqrt{\Psi - \mathcal{E}} f(\mathcal{E}) d\mathcal{E}$$

In the last step we write $\rho(\Psi)$ because Ψ is a monotonic function that depends on r, for this reason we can rewrite the density dependence as a dependence on the relative potential.

Then we differentiate both the members using the relative potential: $\frac{d}{d\Psi}$

$$\frac{1}{\sqrt{8}\pi} \frac{d\rho(\Psi)}{d\Psi} = 2 \int_0^\Psi \frac{f(\mathcal{E})}{\sqrt{\Psi - \mathcal{E}}} d\mathcal{E} \tag{2.32}$$

Since the integral is 0 for $\Psi = \mathcal{E}$ we get an integral of Abel which can be inverted:

$$f(\mathcal{E}) = \frac{1}{\sqrt{8}\pi^2} \frac{d}{d\mathcal{E}} \int_0^\mathcal{E} \frac{1}{\sqrt{\mathcal{E} - \Psi}} \frac{d\rho}{d\Psi} d\Psi \ . \tag{2.33}$$

This formula 2.33 is called Eddington's formula and, given a spherical distribution, allows to generate a model with the given density. It is clear that $f(\mathcal{E}) \geq 0$ only if $\frac{1}{\sqrt{\mathcal{E} - \Psi}} \frac{d\rho}{d\Psi} d\Psi \geq 0$, this is a necessary condition. If it is not satisfied the ergodic DF is not compatible with the density distribution $\rho(r)$.

2.5.1 Ergodic DF property

Finally, the ergodic DFs due to the condition on 2.33 show some particular properties.

If we define $E = \frac{v^2}{2} + \Phi(\mathbf{x})$ with $v^2 = v_x^2 + v_y^2 + v_z^2$ then:

$$\overline{v}_i = \frac{1}{n(\mathbf{x})} \int v_i f \left[\frac{1}{2}(v_i^2 + v_j^2 + v_k^2) + \Phi(\mathbf{x}) \right] d^3\mathbf{v} = 0 \tag{2.34}$$

Since $v_i f[\frac{1}{2}(v_i^2 + v_j^2 + v_k^2) + \Phi(\mathbf{x})]$ is an odd function. This is also applied to mixed terms, $i \neq j$:

$$
\begin{aligned}
\overline{v_i v_j} &= \frac{1}{n(\mathbf{x})} \int v_i v_j f \left[\frac{1}{2}(v_i^2 + v_j^2 + v_k^2) + \Phi(\mathbf{x}) \right] \mathrm{d}^3 \mathbf{v} \\
&= \frac{1}{n(\mathbf{x})} \int \mathrm{d}v_k \int v_j \mathrm{d}v_j \int v_i f \left[\frac{1}{2}(v_i^2 + v_j^2 + v_k^2) + \Phi(\mathbf{x}) \right] \mathrm{d}v_i = 0
\end{aligned}
$$
(2.35)

For this reason the velocity dispersion tensor contains only the non-mixed second moments:

$$
\sigma_{ii}^2 = \overline{v_i^2} = \frac{1}{n(\mathbf{x})} \int \mathrm{d}v_k \int \mathrm{d}v_j \int v_i^2 f \left[\frac{1}{2}(v_i^2 + v_j^2 + v_k^2) + \Phi(\mathbf{x}) \right] \mathrm{d}v_i \; .
$$
(2.36)

The velocity dispersion tensor is diagonal and symmetrical, the stellar system is isotropic and the velocity ellipsoid at each point is a sphere. Moreover, if the DF is ergodic a self-gravitating system has spherical symmetry:

$$
\overline{v}_r = \overline{v}_\theta = \overline{v}_\phi = 0 \quad ; \quad \sigma_r^2 = \sigma_\theta^2 = \sigma_\phi^2 = \sigma^2 \; .
$$
(2.37)

Chapter 3

N-body models of the Fornax dSph

In this chapter we present models with a Fornax-like density profile. We show two models: a Navarro-Frenk-White with core (NFWc hereafter) with analytic density distribution and the P18 model, which is a model with numerical density distribution in which the density profile is taken from the numerical model of (36).

For simplicity we will limit ourselves to building a non-rotating and spherical model. A rotating and non-spherical model would certainly be more realistic but would introduce complications on a mathematical and physical level that are not necessary for our purpose.

Once the model parameters have been chosen, we will construct N-body realizations of the models using an ergodic distribution function (section 2.5).

We will then run a simulation in isolation of the model with the `FVFPS` colissionless code (28) to assess how the equilibrium is maintained numerically. The sample of particles should already be in equilibrium since the coordinates of velocity and position of the particles have been extracted from a DF (section 2.4). However, deviations from an exact equilibrium are expected due to discreteness effects.

As previously mentioned in section 1.1, the density profile in dSph is often dominated by dark matter, and in the case of Fornax this dominates at all radii (36). This is supported by studies that exploit different methods to investigate the dynamics of the satellite. Dynamical models of Fornax suggest that the DM halo has a central core (36), (10), (6), (3), (1).

The data in our possession, and which provide us the observational Fornax constraints, are those provided by (36). The data concern the total

density profile, the dark matter density profile and the stellar density profile with relative errors, are summarized in figure 3.1. We also report fig 2 from (36) (see fig 3.2) with the comparison between the real data and the Fnxcore3 model.
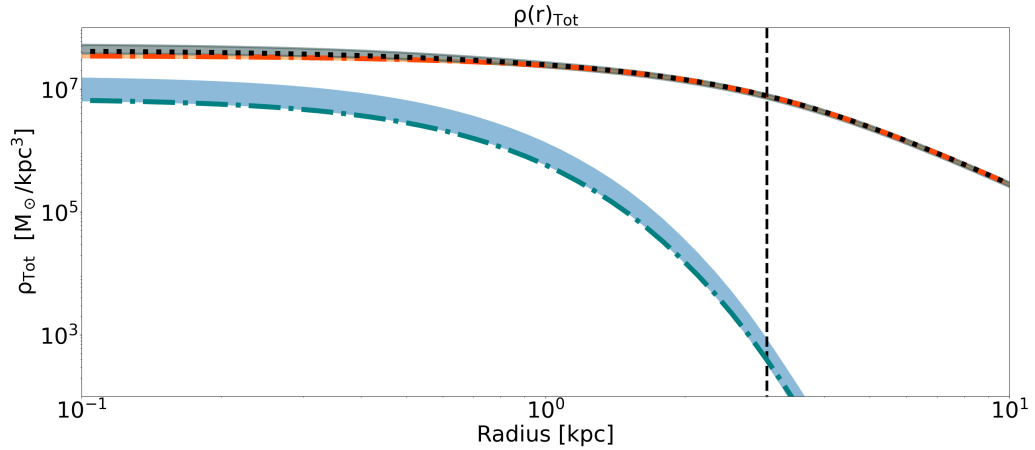

Figure 3.1: Density profile of Fornax component from (36). The black line: total density profile. The orange line: dark matter density profile. The blue line: stellar density profile. The shade represents the Poissonian error. The black vertical dashed line indicates 3 kpc.
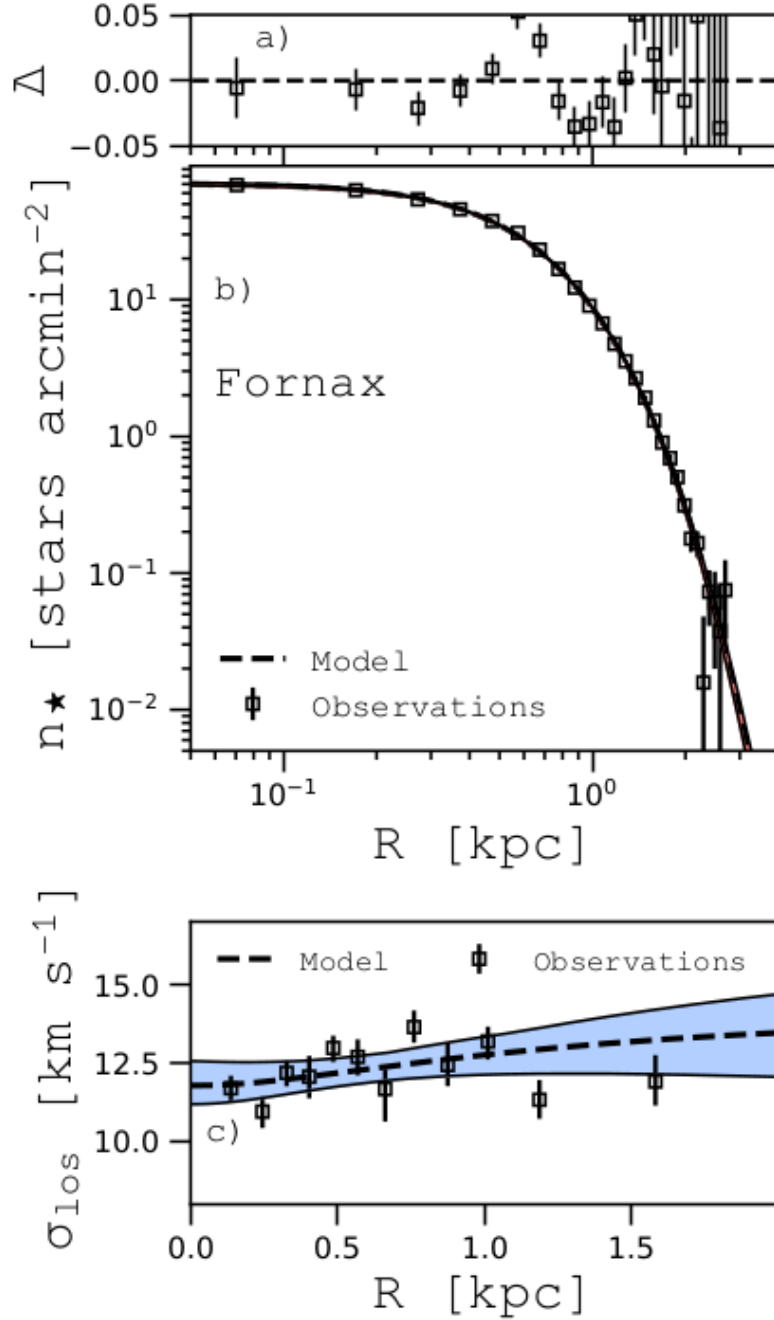
Figure 3.2: Panel a: residuals $\Delta = (n_\star^{\mathrm{obs}} - n_\star)/n_\star$ between the best model (FnxCore3) and the observed projected stellar number density profiles ($n_\star^{\mathrm{obs}}$, dashed curve). Panel b: projected number density profile of the best model (dashed line) compared with the observed profile (points with error bars). Panel c: line-of-sight velocity dispersion profile of the best model compared with the observed profile (points with error bars). Bands show the 1σ un-certainty. Note that the x-axis is logarithmic in panel b and linear in panel c. The figure is from (36).

3.1 Model with analytic cored NFW total density distribution

The NFW is a model presented in (34) that describes the cold dark matter halos of systems close to equilibrium.

In general dark matter halos show a density profile similar to that of the isothermal sphere at intermediate radii, shallower then r^{-2} towards the center and steeper then r^{-2} near the r_{vir}.

The NFW model describe these deviations from the density profile of the isothermal sphere, for this reason is the standard model used in the description of this structures. However, the NFW model is created to describe cold dark matter halos as obtained in dark-matter only cosmological simulations. For this reason it does not take into account the peculiarities due to star formation of the host galaxy, which can cause the halo to deviate from an NFW pattern. An example of this interaction are dwarf galaxies (33).

In order to best describe these deviations, the cored NFW (NFWc hereafter) was created (34). Specifically, to describe the profiles of dwarf galaxies which, through the study of kinematic tracers, such as rotating gas disks, show a flat density profile in the center not compatible with the classic NFW (12).

Fornax is a dwarf galaxy but it is also a satellite of the Milky Way that has undergone an evolution probably experiencing phases of non-equilibrium. To try to maintain some flexibility on the importance and size of the core within the halo, we use the density profile used in (20):

$$\rho_{\text{DM}}(r) = \frac{\rho_{\text{crit}}\delta_c}{\left(1 + \frac{r}{r_s}\right)^2 \left(\frac{r_c^2 + r^2}{r_s^2}\right)^{\frac{1}{2}}} \ , \tag{3.1}$$

$$\text{where } \rho_{\text{crit}} = \frac{3H^2}{8\pi G} \quad , \quad \delta_c = \frac{200}{3}\frac{c^3}{\ln\left(1+c\right) - c/(1+c)} \quad , \tag{3.2}$$

r_s is the scale radius, (such that $\text{d}\ln\rho_s/\text{d}\ln r = -2$); r_c is the core radius (which describes the central region where the profile is flat); c=r_{200} is the concentration parameter; δ_c is the overdensity and ρ_{crit} the critical density of the universe.

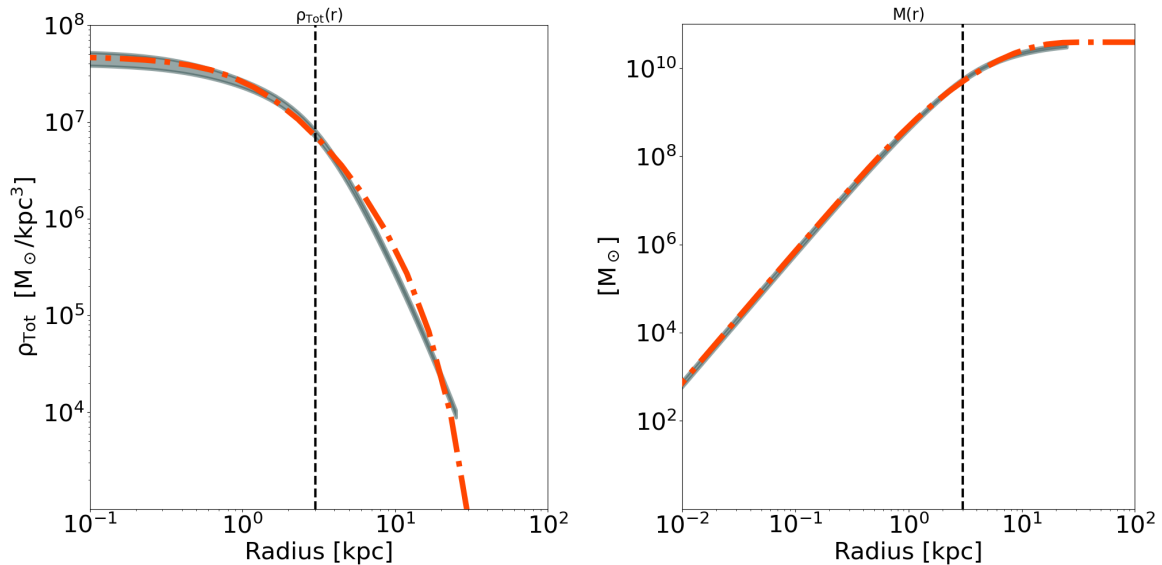An example is available in the figure 3.3 with its parameter table 3.1.

Figure 3.3: Left: total mass density profiles of the Fornax dSph. In gray the density profile provided by (36), the width of the line represents its error. In orange the analytical density profile of the NFWc eq 3.1 Right: cumulative mass function of the Fornax dSph. In gray the cumulative mass function extrapolated from (36) data. In orange the cumulative mass function of the NFWc eq 3.1. The parameter of the NFWc model in figure are in table 3.1. The black vertical dashed line represents 3 kpc.

The profile is in excellent agreement with the data at $r < 5$ kpc, while there is some deviation at larger radii. However, the most important region for us is the one within 3 kpc where we find most of the stellar component (4). A small deviation from the reference profile in the outer regions is acceptable, because it is less important for our purpose and it should have no consequences for our results.

M_{200}	$4 \cdot 10^{10}$	$M_\odot$
r_c	1.1	kpc
r_t	15	kpc
$r_{\text{half mass}}$	7.727	kpc
h	0.67	$H/100$
t_{dyn}	$2.1 \cdot 10^{-1}$	Gyr

Table 3.1: M_{200}, mass at the radius where the density reaches 200 times the critical density of the Universe. r_c and r_t are defined in eq 3.1. h, normalized Hubble constant. t_{dyn}, dynamical time (eq 2.13). $r_{\text{half mass}}$, represents the radius enclosing half the mass of the satellite.

3.2   Model P18 with tabulated total density distribution

The P18 model is created from density tables. The orange density profile in figure 3.4 is obtained using data taken from (36) multiplied with an exponential drop: $\exp\left(-\left(\frac{r}{r_t}\right)^2\right)$, where r_t is the truncation radius. Other important parameters are M_{200} and r_s (tab 3.2) which allow to raise/lower the orange curve in figure 3.4. These two parameters were taken from the FnxCore3 model presented in (36).
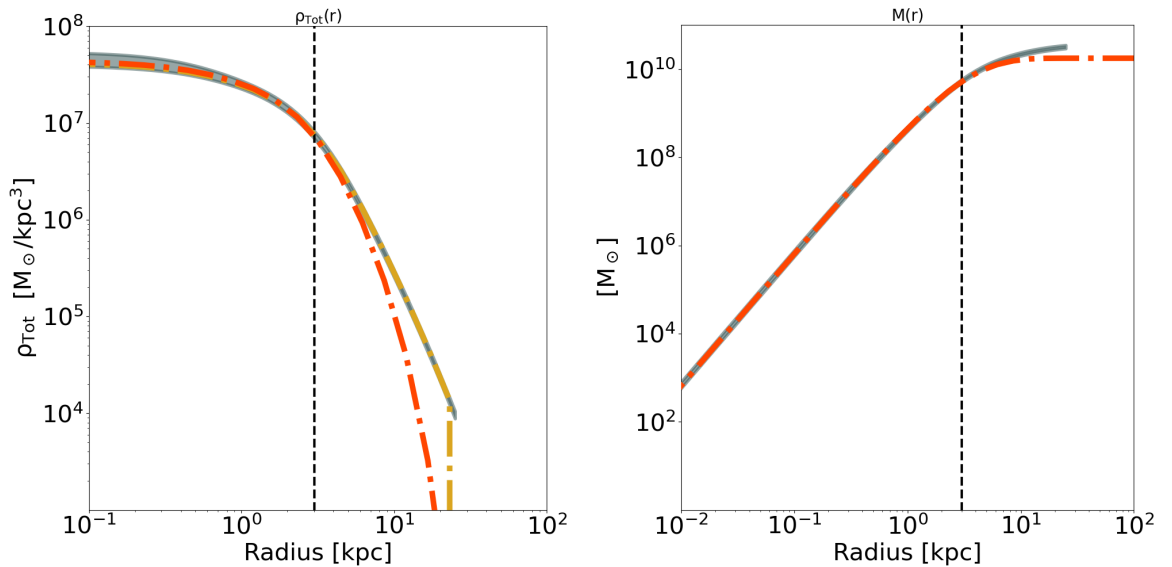

Figure 3.4: Same as fig 3.3 but for the P18 Model. Yellow line: P18 model without exponential cut off.

M_{200}	$1.44 \cdot 10^9$	$M_\odot$
r_s	3	kpc
r_t	10	kpc
$r_{\text{half mass}}$	4.310	kpc
t_{dyn}	$1.3 \cdot 10^{-1}$	Gyr

Table 3.2: M_{200} is the mass within a sphere of radius r_s. r_s is the scale radius. t_{dyn}, dt and $r_{\text{half mass}}$ are the same as in tab 3.1.

A detail that catches the eye of the model in fig 3.4 is the vertical fall around ~ 23 kpc of yellow line. This fall is due to the nature of the model, when the density table stops so does the model without exponential falls to mitigate. Such an abrupt transition can produce undesirable effects that will emerge and can evolve in the simulation in isolation. In order to mitigate this effects we introduced the exponential cut off.
As we see this solution has its drawback, there is a slight deviation from the reference profile in the outermost areas. But, as already said for the NFWc model, these deviations in the external areas are not very significant.

3.3   N-body simulations of the isolated models

In this section we illustrate the result of the evolution of the P18 model in isolation, P18-IS simulation (fig 3.5), and the evolution of the NFWc model in isolation, NFWc-IS simulation (fig 3.6).
The simulations last 12 Gyr in an environment without external potential or external influences of any kind. 12 Gyr is chosen as the reference time because it is a much longer time than their dynamical time (NFWc Tab 3.1, P18 model Tab 3.2). In this way we can can asseses the numerical effects on the equilibrium of the model.
The main indicators that we monitor in the simulation are $r_{\text{half mass}}$ (NFWc Tab 3.1 and P18 model Tab 3.2), ρ_{150} variations and, more specifically, the density profile.
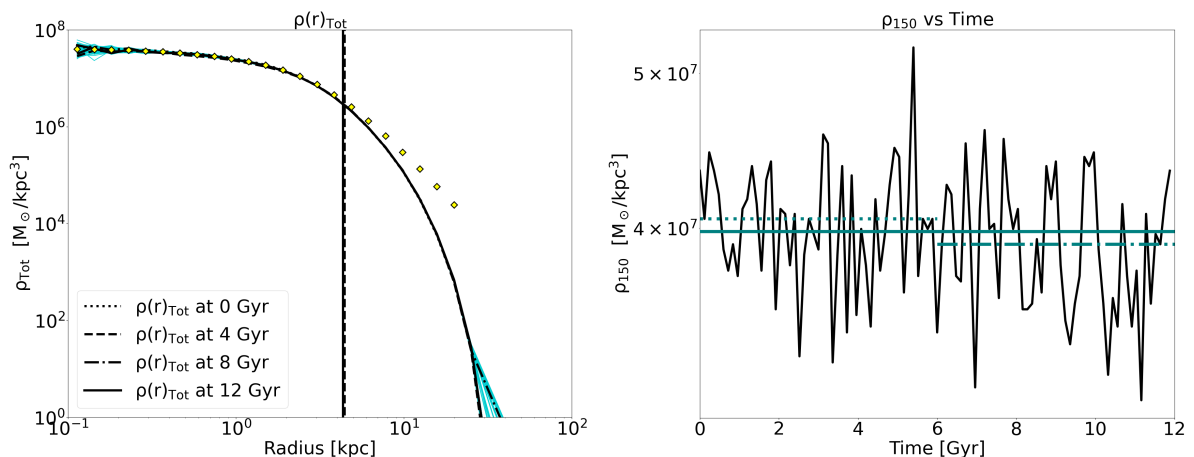
Figure 3.5: Left: P18 model density profile evolution in 12 Gyr. Cyan line: density profile plotted at each dt. Black line: profile at fixed time: 0, 4, 8, 12 Gyr. Yellow diamonds: total density profile from (36). Black vertical line: largest and smallest $r_{\text{half mass}}$ found.
Right, ρ_{150} variation in 12 Gyr of evolution. Blue dotted line: median between 0-6 Gyr. Blue dashed line: median between 6-12 Gyr. Blu solid line: median 0-12 Gyr.

In fig 3.5, of the P18-IS simulation, the only significant variation occurs in the tail of the density profile. However the densities are low and therefore the impact is not very significant. The reason for this deviation is probably due to numerical effects. These effects are not strong enough to become artificial mass loss effects. The result after 12 Gyr of evolution is the shape of that tail at low densities and high distance from the centre
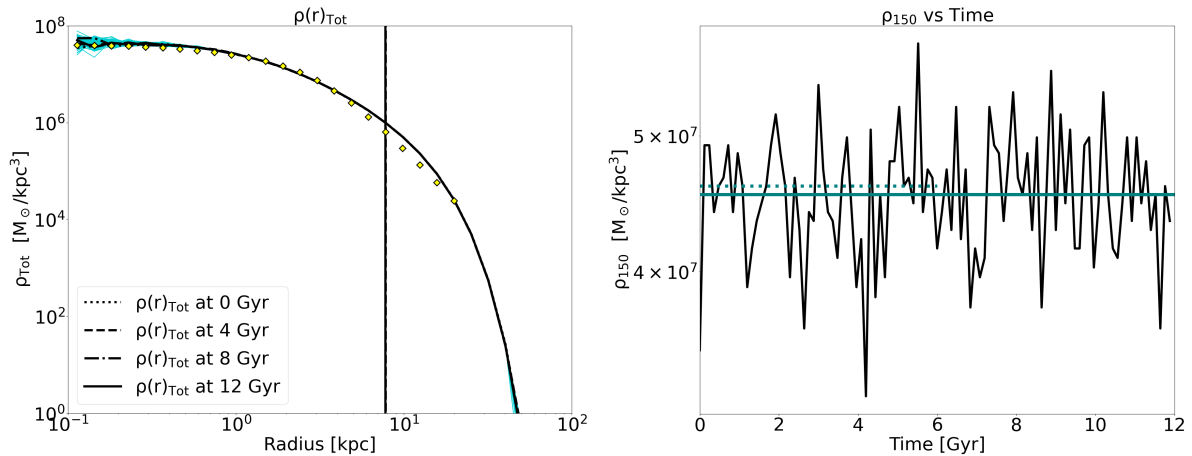
Figure 3.6: Same as fig 3.5 with the NFWc model.

of the system which does not appear to affect the model in any other way. Furthermore, $r_{\text{half mass}}$ and ρ_{150} show small oscillations but remain virtually unchanged over the course of evolution. Since these variations are not significant, conclude that our realization of the P18 model has negligible numerical effects.

The tail is instead absent in the NFWc-IS simulation, fig 3.6, as it is well described also in the outermost parts and shows no signs of variation.

One last method of verification that we can adopt is a visual method, we can observe the X-Z and Y-Z planes for the two models (fig 3.7 and 3.8). We expect the conservation of their spherical shape throughout the simulation since the $\overline{v}_i = 0$, see subsection 2.5.1.
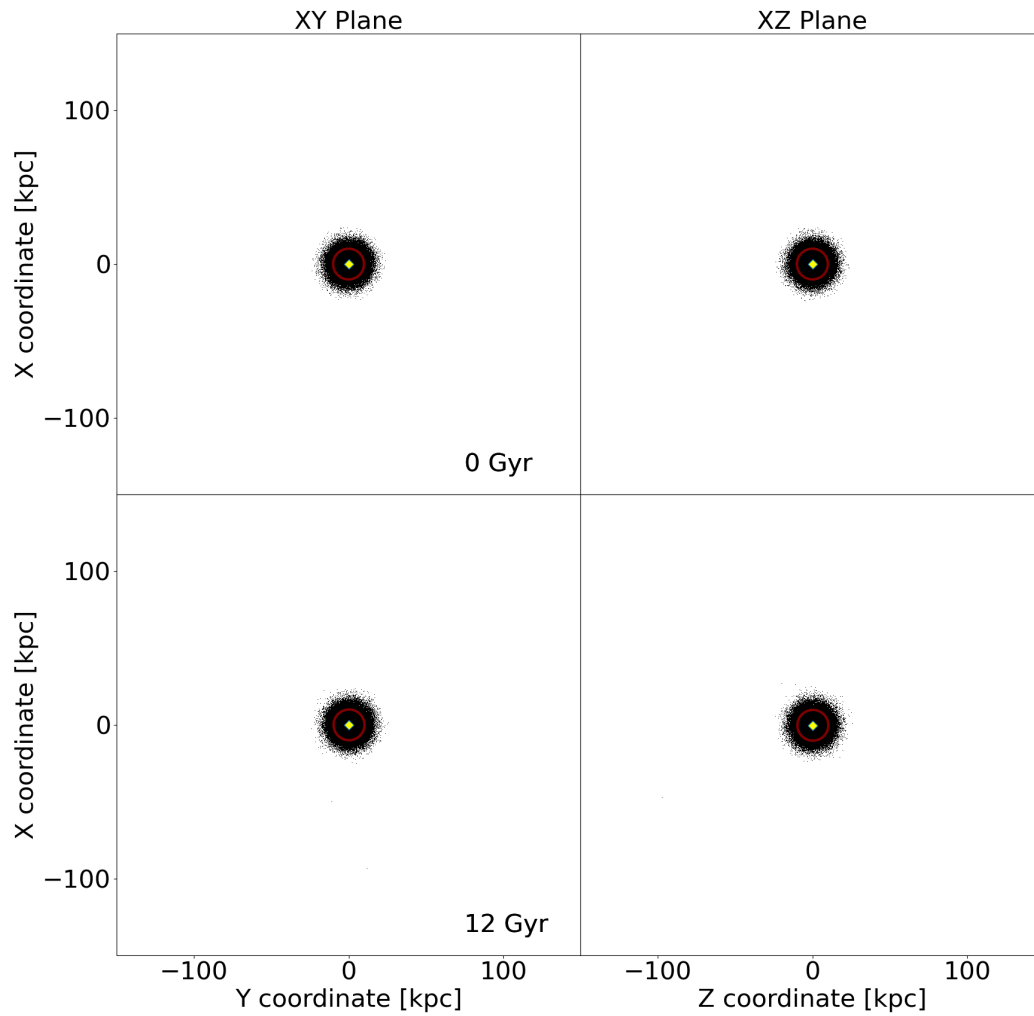
Figure 3.7: Spatial distribution of the particles of the satellite at different times in different planes for the P18-IS simulation. Blacks dot: particles. Yellow diamond: centre of mass now. Red circle: circle with a radius of 10 kpc as reference.
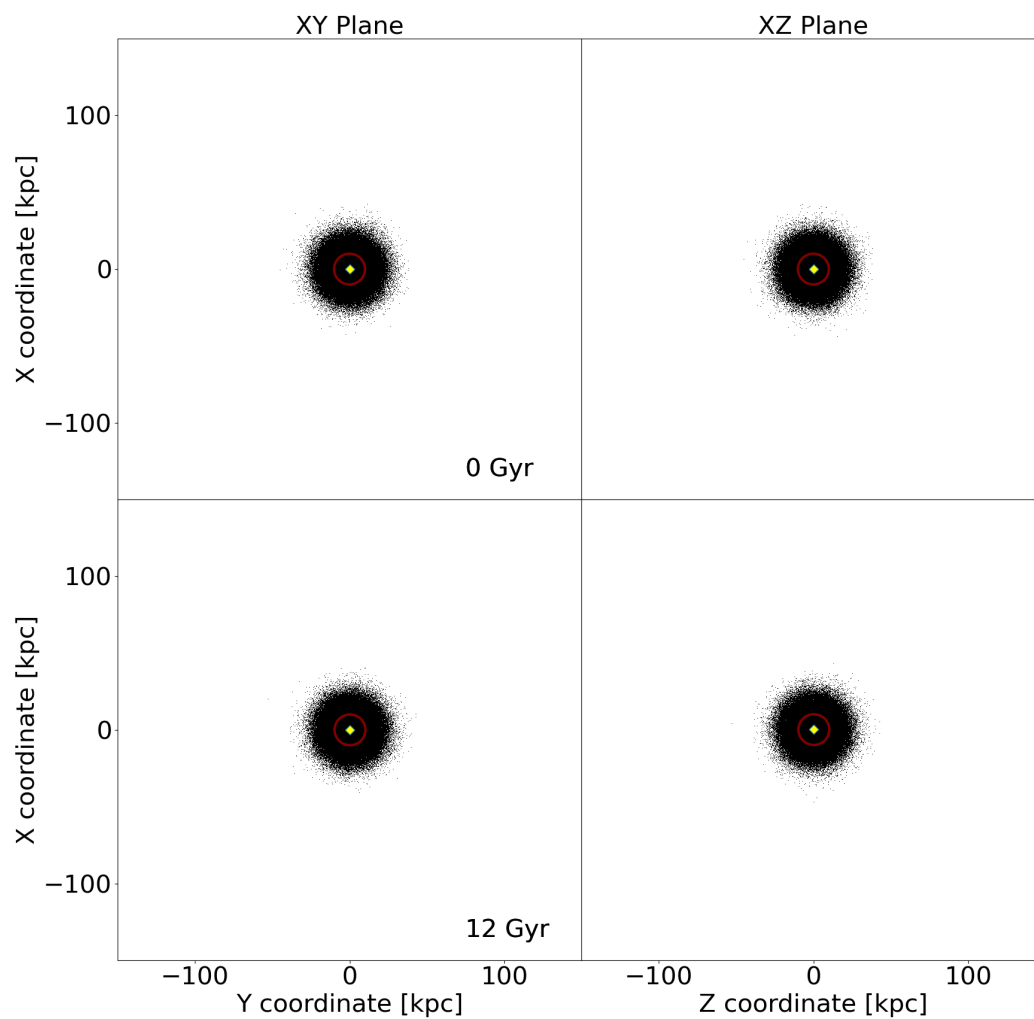
Figure 3.8: Same as fig 3.7 for the NFWc-IS simulation.

In conclusion, our N-body models behave well when evolved in isolation. Thus, we can safely use them in simulations in which we will study the evolution of Fornax orbiting the Milky Way.

Chapter 4

Effective N-body models of composite collisionless stellar systems

The purpose of this chapter is to illustrate how it is possible to create two new components from a simulation of a N-body system made with a single component.

We will define a probability function $\mathcal{P}_k(\mathcal{I})$, we will divide the mass of each particle into fractions, each fraction will be representative of a different component. By adding the mass fractions corresponding to the same component we can build a density profile. We will get two different density profiles and we can change them without repeating the simulation but only by changing *a posteriori* the probability function.

For this reason all simulations are done with a single collisionless component so we do not have an initial distinction between the stellar component and the dark matter. In this chapter different functions are shown that allow us to create components with different characteristics, this also allows us to demonstrate the flexibility of the method.

4.1   Distribution functions and portion functions

Every single particle is generated with an initial energy, given by the sum of its gravitational potential energy and its kinetic energy. In fig 4.1 we show two examples of initial energy distribution.

When we refer to initial energy we refer to the energy of the particles when the satellite is set up in equilibrium and isolated. This energy does not depend only on the particle position, but is somewhat representative of the region in which the particle is located. The higher the energy, in absolute value, the more likely it is to be in the central regions of the satellite, where we expect to find the most bound particles.
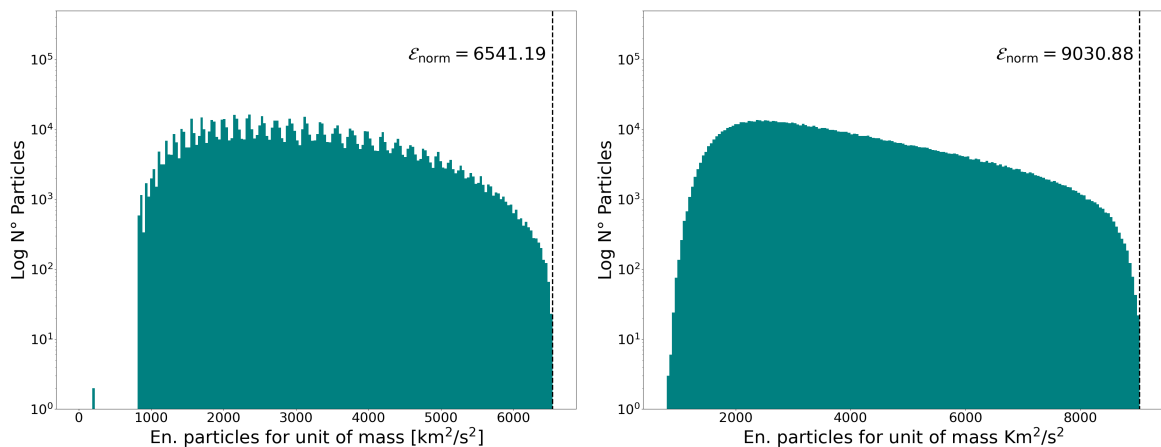

Figure 4.1: (Left) P18 model (section 3.2) initial distribution of energy in isolation. (Right) NFWc (section 3.1) initial energy distribution in isolation. Black vertical dashed line: represents $\mathcal{E}_{norm}$, $\mathcal{E}$ of the highest-$\mathcal{E}$ particle section 4.2. The shape of the distribution is model and mass dependent. Here $\mathcal{E} = -E$

.

In order to separate the components we need to define a function that we will call $\mathcal{P}_k(\mathcal{I})$, where $\mathcal{I}$ is an integral of motion, in our case the initial energy (35). This $\mathcal{P}_k(\mathcal{I})$ corresponds to the probability, based on the chosen integral of motion, that a particle belongs to one component rather than another. This function is such that:

$$\mathcal{P}_k(\mathcal{I}) = \frac{f_k(\mathcal{I})}{f_{\text{tot}}(\mathcal{I})} \text{ , where } f_{\text{tot}}(\mathcal{I}) = \sum_{k=1}^{N_{\text{comp}}} f_k(\mathcal{I}) \tag{4.1}$$

is a DF of a stationary collisionless stellar systems obtained from Jeans theorem, see section 2.4, (5). By definition:

$$\sum_i^{N_{\text{comp}}} \mathcal{P}_k(\mathcal{I}) = 1 \qquad (4.2)$$

where N_{comp} is the number of components and f_k is the DF to the $k - th$ component. The probability:

$$\mathcal{P}_k(\mathcal{I}_i) = \xi_{k,i} \qquad (4.3)$$

that a particle belongs to the $k - th$ component is converted into a mass fraction so that

$$\mathcal{M}_k = \sum_i \xi_{k,i} m_i \qquad (4.4)$$

is the total mass of the $k - th$ component, m_i the total mass of the $i - th$ particle and $\xi_{k,i}$ is the mass fraction of the $i - th$ particle that belongs to the $k - th$ component.
With this method we can construct two $\mathcal{P}_k(\mathcal{I})$.
The first is representative of the stellar component $\mathcal{P}_\star(\mathcal{I})$ and the second represents the dark matter component $\mathcal{P}_{\text{DM}}(\mathcal{I})$, with $\mathcal{P}_\star(\mathcal{I}) + \mathcal{P}_{\text{DM}}(\mathcal{I}) = 1$. Now, we can proceed to calculate the density profile with a basic shell-counted method. We divide the space into spherical shells centered in the system's centre of mass and then count the numbers of particles in each shell. Finally we associate to each particle its mass based on which component we are considering.
With the simple but powerful method described in section 4.1 we can create for instance the stellar component of a galaxy and follow its time evolution. We can reinterpret the same simulations with different $\mathcal{P}_k(\mathcal{I})$. In our case the observational data are those provided from (36), which give us constraints on the stellar and dark matter density profile, see fig 3.1.
Now, we need to find the $\mathcal{P}_k(\mathcal{I})$ that best suits these requests. Hereafter we assume $I = \mathcal{E}$, where $E = -\mathcal{E}$ is the relative energy per unit mass, and we focus on the stellar component.

4.2 Choice of the stellar portion function $\mathcal{P}_\star(\mathcal{E})$

This section presents two different $\mathcal{P}_\star(\mathcal{E})$, one taken from (35) and the other constructed in this work. Both satisfactorily the given observational constraints, demonstrating that there are more $\mathcal{P}_\star(\mathcal{E})$ that can reproduce the same observables.

There are therefore many ways to build the $\mathcal{P}_\star(\mathcal{E})$ that is most suitable for us. One of the possible standards is to use the generalized Schechter function already exposed in (35) with an appropriate parameter calibration.

This functional form is very convenient because it is quite flexible thanks to the four parameters that regulate the curve.

This is the $\mathcal{P}_\star(\mathcal{E})$ used in (35):

$$\mathcal{P}_\star(\mathcal{E}) = A \left(\frac{\mathcal{E}}{\mathcal{E}_0}\right)^\alpha \exp\left[-\left(\frac{\mathcal{E}}{\mathcal{E}_0}\right)^\beta\right] \qquad \text{with} \qquad \mathcal{E}_0 = -E_0 \ . \qquad (4.5)$$

This function has four parameters: A, α, β and $\mathcal{E}_0$. Each of the parameters has its own influence on the shape of the final curve.

Note that $\mathcal{E}_0$ is a fixed relative energy which we can choose and $\mathcal{E}$ is the energy of the particles. We express $\mathcal{E}_0$ in unit of a normalization energy $\mathcal{E}_{\text{norm}} = \Psi_0$, where Ψ_0 is the value of the central gravitational potential Ψ taken positive (assuming $\Psi \to 0$ for $r \to \infty$). We will therefore write $\mathcal{E}_0 = 0.7$ meaning that it 70% of $\mathcal{E}_{\text{norm}}$.

One thing to note is that the shape of the density profile for the stellar component is not easily predictable. Unless we choose to use a very simple $\mathcal{P}(\mathcal{E})_\star$ (see fig 4.2), such as:

$$\mathcal{P}_\star(\mathcal{E}) = \Theta(\mathcal{E}) \begin{cases} 0, & \mathcal{E} < 5000 \\ 1, & \mathcal{E} \geq 5000 \end{cases} \qquad (4.6)$$

Where all and only the particles with a energy higher than a given value contribute to the mass of the component.

This happens because we are going to act on the mass fraction that each particle gives to a certain component and the particles are not spatially well distinct. The highest-$\mathcal{E}$ particles are expected to be found in the innermost region of the satellite. But these particles are not static and are mixed with low-$\mathcal{E}$ particles. This mixture varies with the distance from
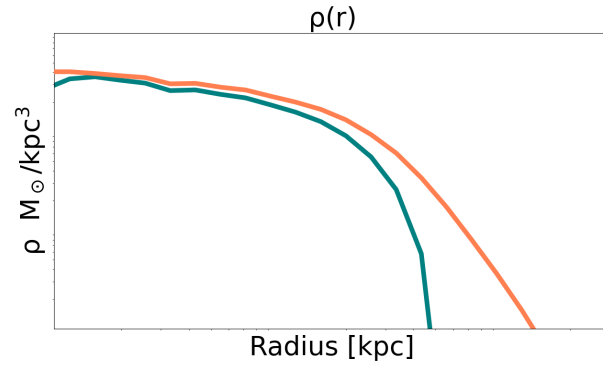
Figure 4.2: Blue: example of component obtained with the $\mathcal{P}(\mathcal{E})_\star$ given by eq 4.6 applied to P18 model. Orange: total density profile.

the center, because in the outermost regions we expect to find mainly low-$\mathcal{E}$ particles. Therefore, the greater the complexity of the $\mathcal{P}(\mathcal{E})$, the more complex it is to predict the behavior of the profile.

The most useful thing we can do is to study, one at a time, the influence of the parameters of eq 4.5 on our dataset, see fig 4.3.
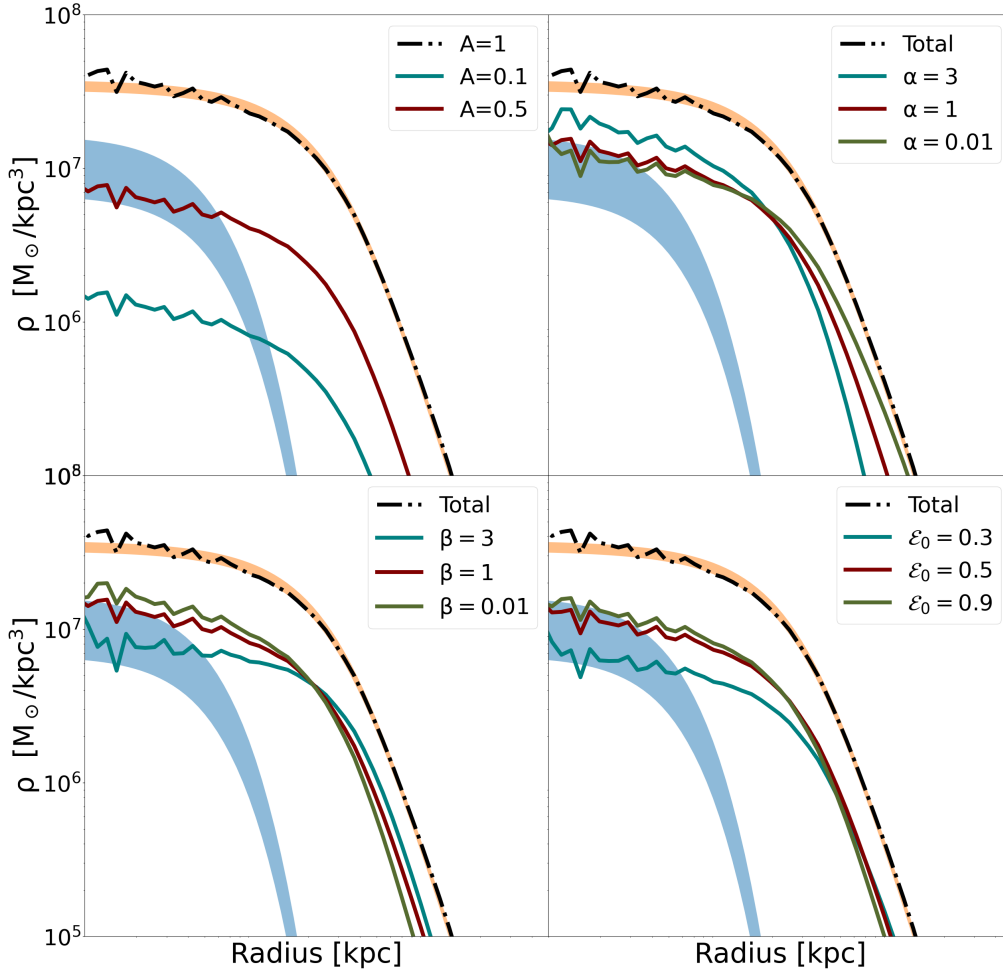
Figure 4.3: Orange and Blue are represents the profile data from (36), see fig 3.1. Black line: represents the density profile obtained from the P18-IS simulation. Red, Green, Blue line: stellar density profiles obtained from different $\mathcal{P}_\star(\mathcal{E})$, from Eq 4.5, according to the variation of a specific parameter indicated in the legend. Where not specified the parameters are set to: A=1, $\alpha = 1$, $\beta = 1$, $\mathcal{E}_0 = 0.7$.

As we can see from the figure 4.3, the different parameters lower the curve in different ways. Each parameter flattens the curve slightly differently and affecting, or not, the large radius tail. Their appropriate combination can allow us to describe the blue area, which is the stellar component we aim to reproduce in our application.

For example, to satisfy our current constraints, this set of parameters works:

$$A = 0.22, \qquad \alpha = 25, \qquad \beta = 0.5, \qquad \mathcal{E}_0 = 0.9. \qquad (4.7)$$

Its application can be seen in fig 4.4, the initial distribution of probability can be seen in fig 4.5.
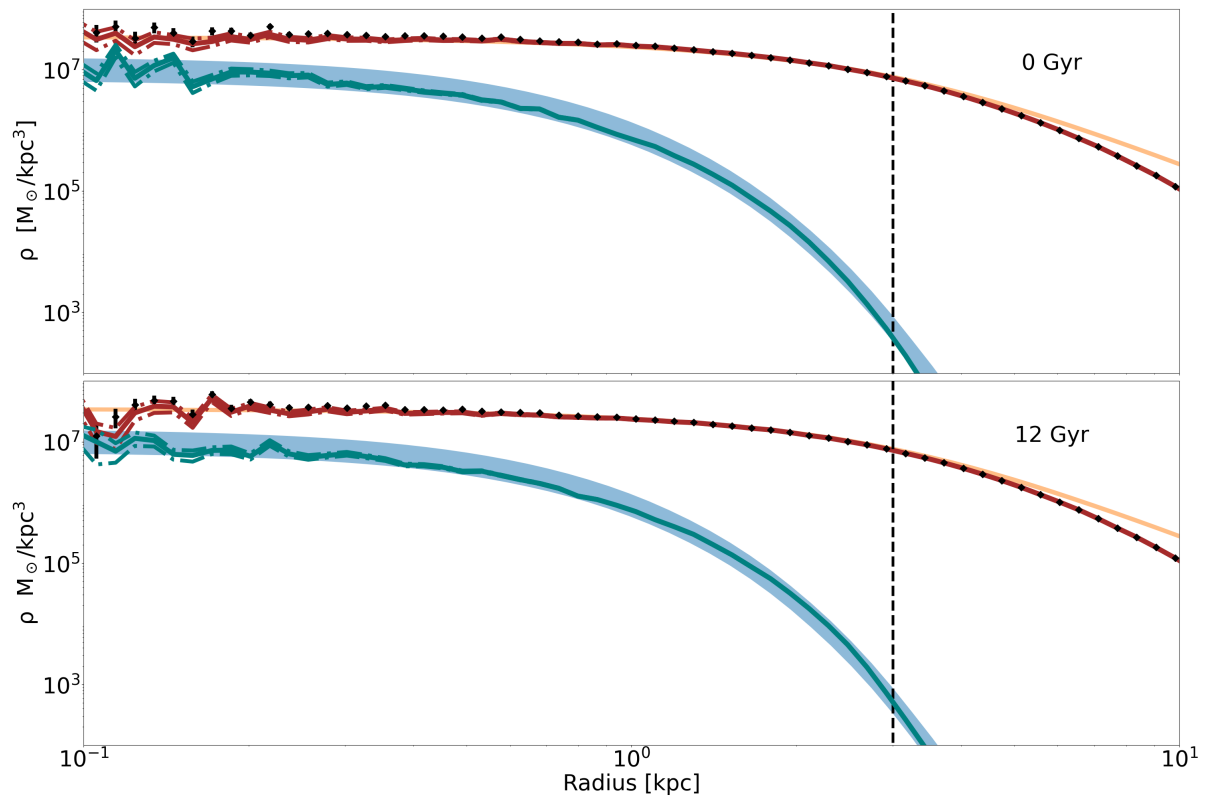
Figure 4.4: Density profiles of the P18-IS simulation. Blue solid line: represent the stellar density profile. Red solid line: represent the dark matter density profile. Black dots: total density profile. Orange and blue area: dark matter and stellar density profiles from (36), see fig 3.1. The colored dashed lines are representative of the associated Poisson error.

In figure 4.4 we can see the density profile obtained from the evolution of the P18 model in isolation with the addition of the stellar component. Since the model has already been established to be in equilibrium (see section 3.1), and the overall variation of its density profile in the 12 Gyr has already been shown in fig 3.5, we expect that there will be no variation between the profile of the stellar component at t = 0 Gyr and that at t = 12 Gyr. We already seen that ρ_{150}, which measures the density variation at 150 pc from the center, did not show significant variations. Therefore, the comparison between the stellar profiles of the two figures is a further confirmation that the equilibrium condition is well maintained.

Furthermore, the equilibrium condition is independent of the choice of the $\mathcal{P}_\star(\mathcal{E})$. So, if we choose another functional form and build a new $\mathcal{P}_\star(\mathcal{E})$, which satisfies the observational constraints, the profile we found should remain in equilibrium.

In fig 4.6 we present the density profile described by a $\mathcal{P}_\star(\mathcal{E})$ with a different functional form applied at the P18 model. Its parameters are already written in the form of relative energies and their result is shown in fig 4.6. The function is:

$$\mathcal{P}_\star(\mathcal{E}) = \log_{10}\left(\frac{\mathcal{E}}{3800}\right) \exp\left(\frac{\mathcal{E} - 6350}{280}\right) , \qquad (4.8)$$

which satisfies, as well as the one used in fig 4.4, the observational constraints, see fig 4.5.
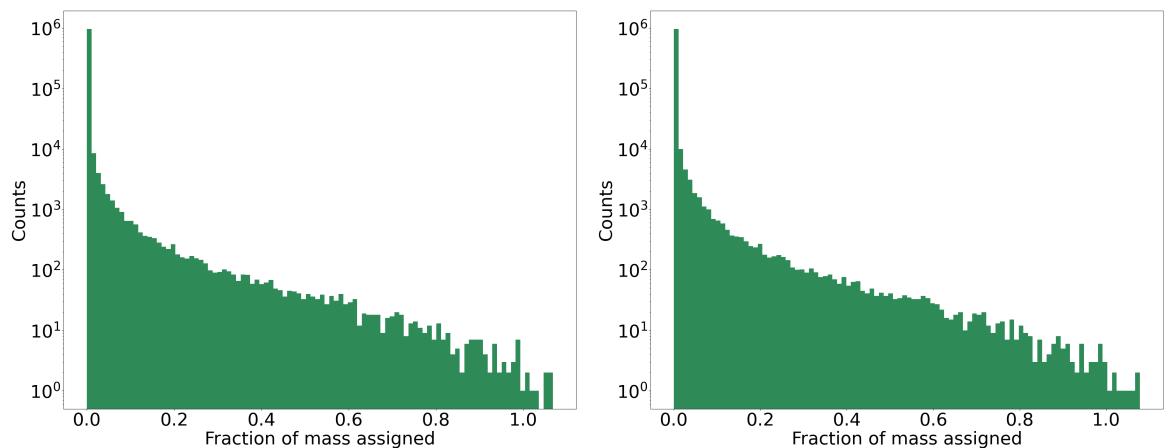

Figure 4.5: Initial distribution of probability of the $\mathcal{P}_\star(\mathcal{E})$ eq 4.7 (left) and eq 4.8 (right)
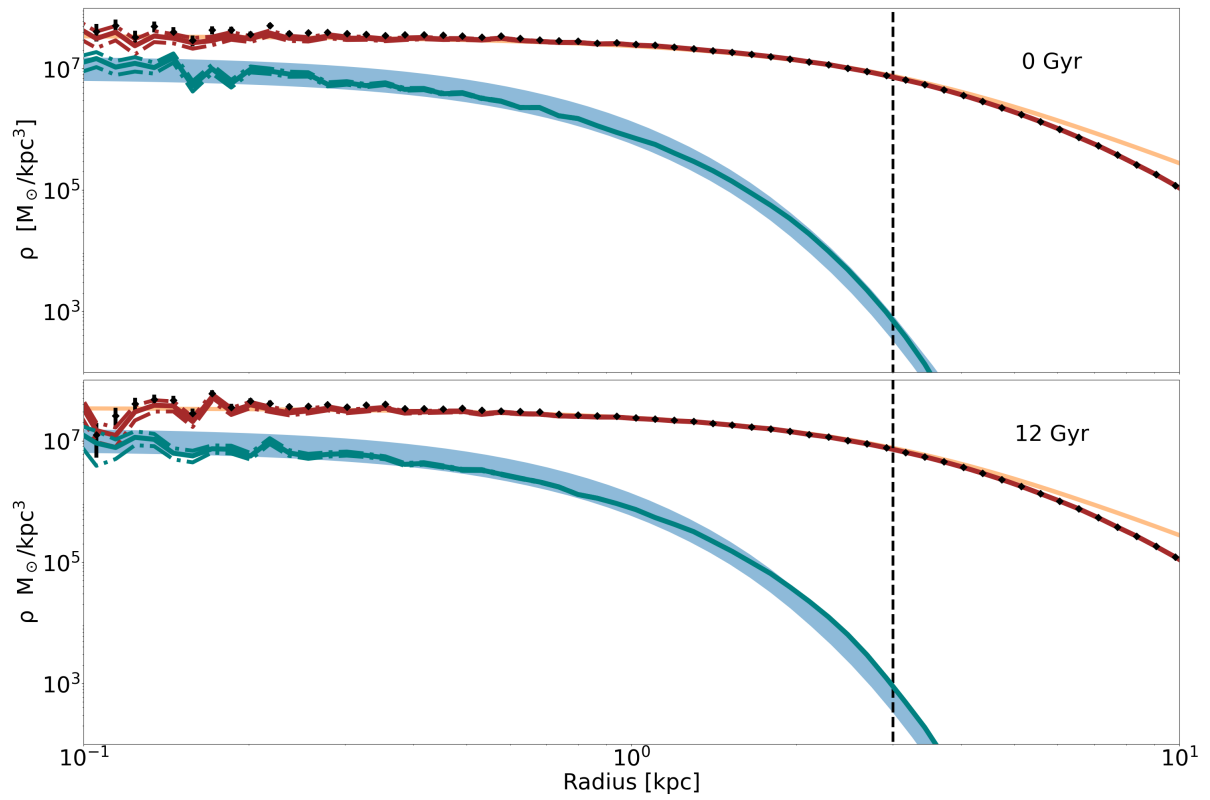
Figure 4.6: Same as fig 4.4 but with the $\mathcal{P}_\star(\mathcal{E})$ in eq 5.4.

Chapter 5

Dynamical evolution of Fornax orbiting the Milky Way

5.1 Initial conditions

In this chapter we illustrate the results obtained in N-body simulations in which Fornax-like satellite evolving in the Milky Way gravitational potential J95, which we describe in section 5.2.

The orbit parameters used for all simulation are shown in table 5.1, they correspond to the orbit named P07ecc in Battaglia et al (2015) (4) presented as the most eccentric orbit consistent with the observational data.
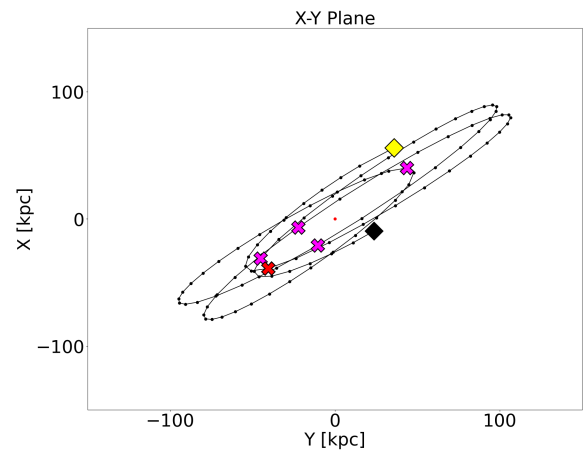
	X coordinate	Y coordinate	Z coordinate	Value	
Position	35.8140	0.0000	137.3890		kpc
Velocity	-94.8750	-77.8100	2.9010		km/s
Perigalactic d.				61	kpc
Eccentricity				0.4	

Table 5.1: Initial conditions of the P07ecc orbit. Position and velocity are relative to the Galactic center.
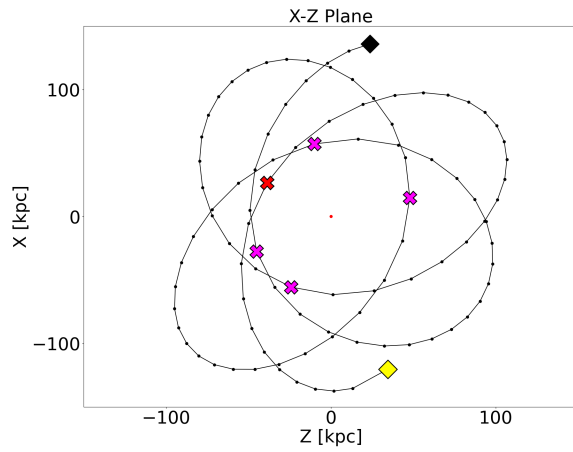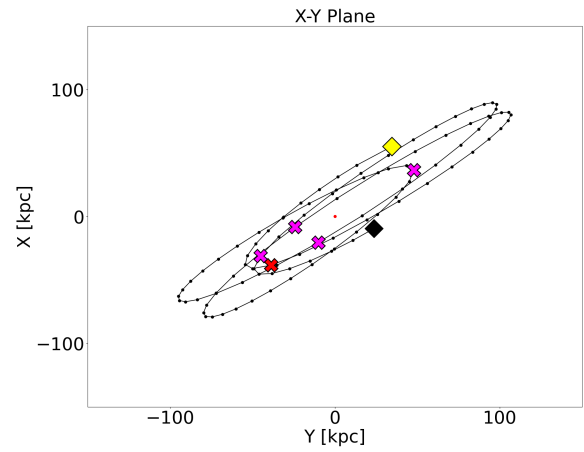
The P07ecc orbit pattern is shown in fig 5.1.
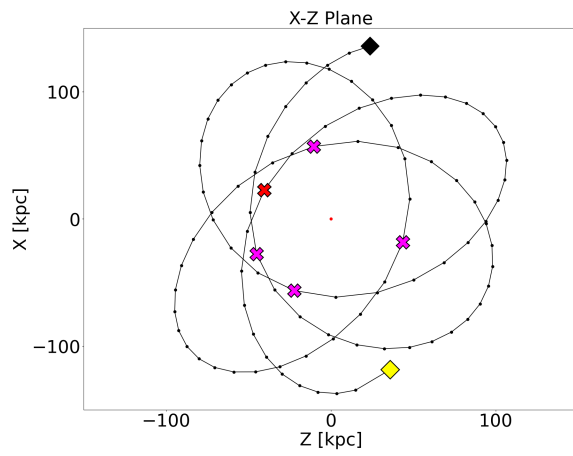
(a) *Pericenter position on X-Z plane, P18-J95 simulation*

(b) *Pericenter position on X-Y plane, P18-J95 simulation*

(c) *Pericenter position on X-Z plane, P18m-J95 simulation*

(d) *Pericenter position on X-Y plane, P18m-J95 simulation*

Figure 5.1: Visualization of the pericenters in X-Z plane and X-Y plane of the P18-J95 simulation (a)(b) and P18m-J95 simulation (c)(d).

5.2 The J95 model of the Milky Way gravitational potential

In this section we present the J95 gravitational potential, one of the many Milky Way-like gravitational potential.
The gravitational potential of the Milky Way can be deduced only indirectly from the kinematics of visible tracers such as stars and gas.
Its not fully constrained, and for this reason different models have been proposed. A possible classification of these potentials can be made on the basis of the expected Milky Way virial mass, so we can divide them into (20):

- heavy potential ($M_{200} \geq 2 \cdot 10^{12}$ M$_\odot$)

- intermediate potential ($M_{200} \approx 1 - 2 \cdot 10^{12}$ M$_\odot$)

- light potential ($M_{200} \leq 1 \cdot 10^{12}$ M$_\odot$)

The J95 potential, first presented in (21), is classified as heavy. It has mass of $\simeq 0.5 \cdot 10^{12}$ M$_\odot$ within 50 kpc and $\simeq 2.3 \cdot 10^{12}$ M$_\odot$ within 300 kpc (20). It consist of three components that describe the gravitational potential of the Milky Way bulge, disk and halo (fig 5.2). The bulge is modelled as an Hernquist sphere (eq 5.1), the disk as a Miyamoto-Nagai disk (eq 5.2), and the dark matter halo as a logarithmic potential (eq 5.3):

$$\Phi_{\text{bulge}} = -\frac{GM_{\text{bulge}}}{r + c}; \tag{5.1}$$

$$\Phi_{\text{disk}} = -\frac{GM_{\text{disk}}}{\sqrt{R^2 + (a + \sqrt{z^2 + b^2})^2}}; \tag{5.2}$$

$$\Phi_{\text{halo}} = v_{\text{halo}}^2 \ln\left(r^2 + d^2\right). \tag{5.3}$$

Hernquist	Miyamoto-Nagai	Logarithmic Potential
$c = 0.70$ kpc	$a = 6.50$ kpc	$d = 12.00$ kpc
	$b = 0.26$ kpc	
$M_{\text{bulge}} = 3.4 \cdot 10^{10}$ M$_\odot$	$M_{\text{disk}} = 1.0 \cdot 10^{11}$ M$_\odot$	
		$v_{\text{halo}} = 212$ km/s

Table 5.2: Parameters for the components of the J95 potential.

The total circular speed ($v_{\mathrm{circ}}^2 = \frac{\mathrm{d}\Phi}{\mathrm{d}R}$) obtained from the sum of the three components gives us the total circular speed of the J95 potential (see fig 5.2).
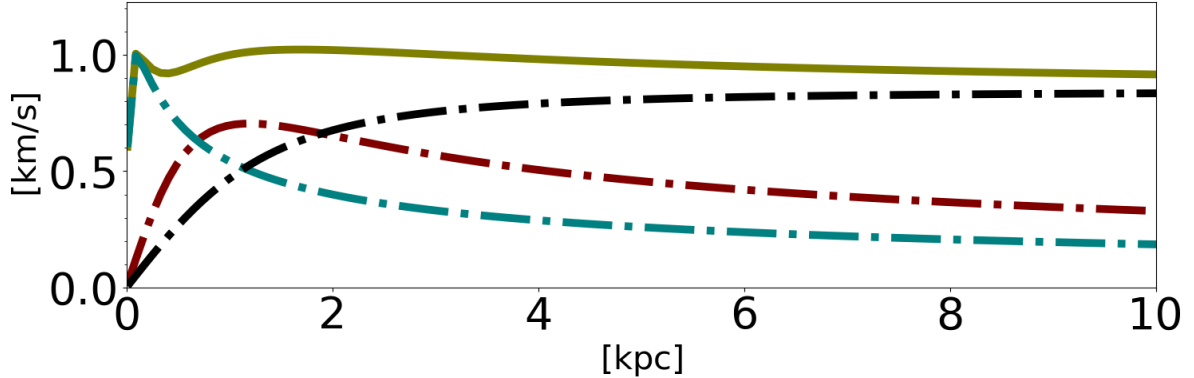

Figure 5.2: J95's potential circular speed produced by the different components. Olive solid line: total circular speed. Red dashed line: bulge circular speed. Blue dashed line: disk circular speed. Black dashed line: halo circular speed. R_0=8 kpc, $V_C(R_0) = 220$ km/s.

The region where the satellite Fornax-like orbits is between 60 kpc and 140 kpc 5.3. This is because the P07ecc orbit (see tab 5.1), used in our simulations, has a pericenter with a perigalactic distance of 61 kpc.
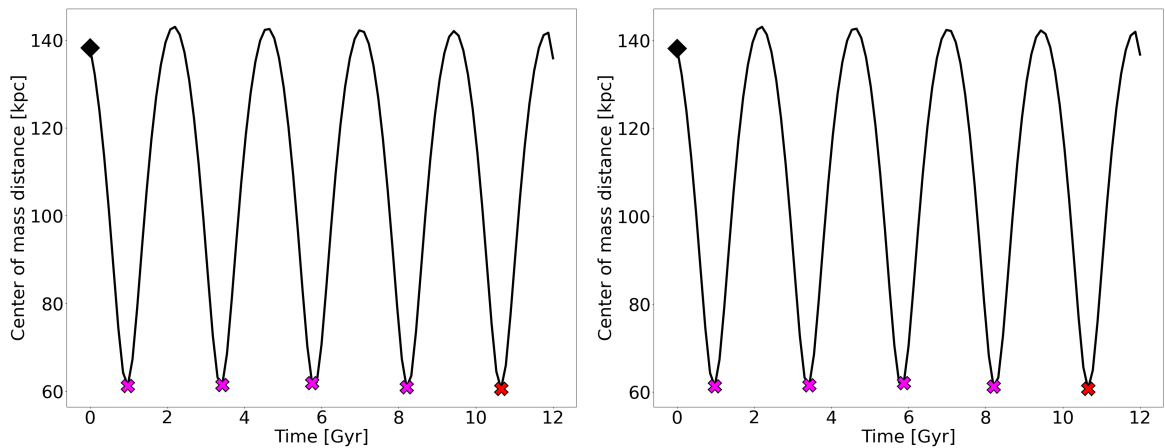

Figure 5.3: Galactocentric distance vs time. Purple crosses: pericenter. Red cross: innermost pericenter. (Left) P18-J95 simulation. (Right) P18m-J95 simulation.

The potential J95 produces an approximately flat circular speed that extends out to 140 kpc 5.4.
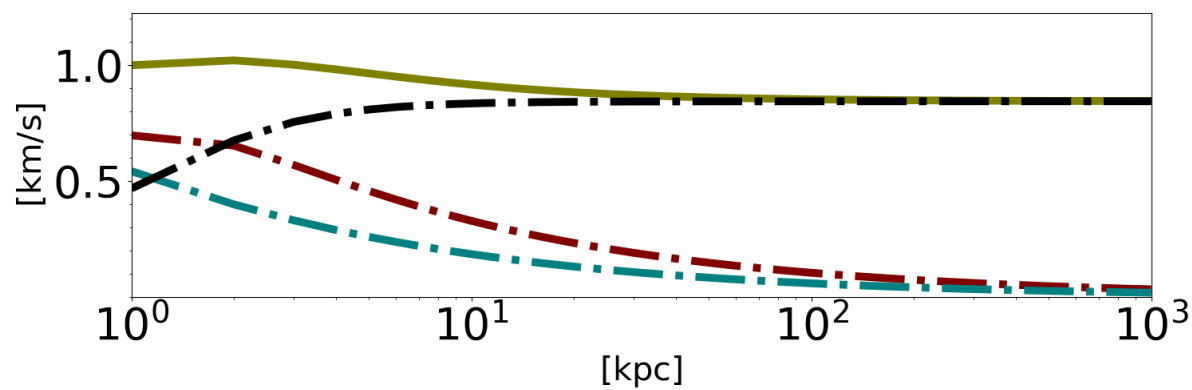
Figure 5.4: Same as fig 5.2. The x-axis is logarithmic.

5.3   Evolution in J95 gravitational Potential

5.3.1   P18 Model

In this section we describe the result of P18-J95 simulation in which the initial satellite density distribution follow the P18 model (see section 3.2). The cyan area of fig 5.5 is created by the superposition of numerous density profiles that have been printed every 0.12 Gyr. This clearly highlights the global shift that the density profile undergoes as it changes over time. The orange line, in particular, represents the density profile at the end of the simulation; we can see how it is below the yellow diamonds that represent the total density profile from the (36) data (see fig 3.1).
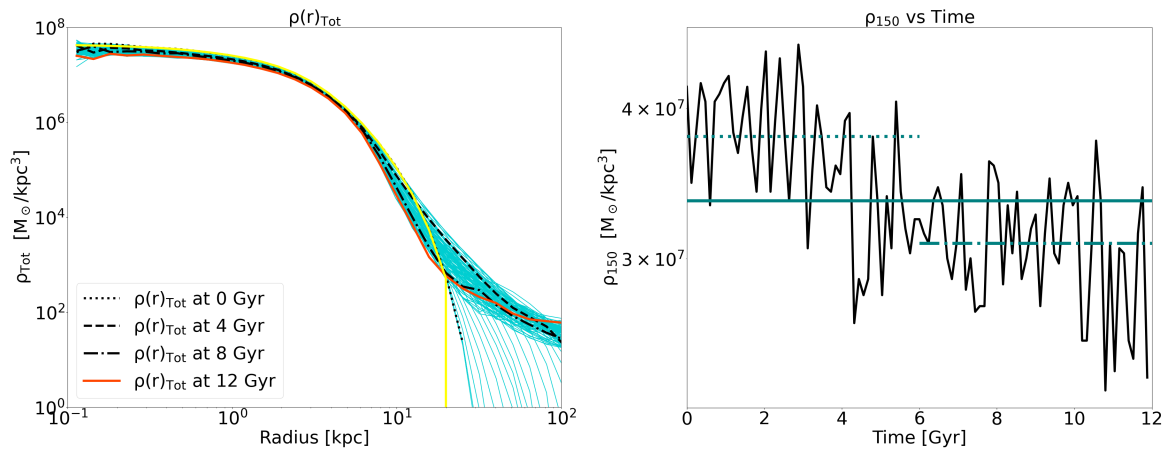

Figure 5.5: (left) Evolution of the total density profile of the satellite in simulation P18-J95. Cyan lines: density profile plotted every 0.12 Gyr. Black lines: profiles at: 0, 4, 8 Gyr. Orange line: profile at 12 Gyr. Yellow line: density profile of the P18 model. (right) ρ_{150} vs time: Same as fig 3.5.

The innermost regions in fig 5.5(right) show small variations of density profile, because the inner regions are strongly bound. The central density remains of the order of 10^7 $M_\odot/kpc^3$ all the time. The big shift occurs at around 10 kpc where the density profile drops down due to the unbound particles.

Due to this mass loss the difference between the simulated profile and the P18 profile increse significally over time. We need to add mass to the initial P18 model to make it more resilient to the tidal stripping. Later in this chapter we will present a model similar to P18 but more massive. In fig 5.6 we show several frames, taken at fixed instants of time (4, 8, 12 Gyr), of the simulation.
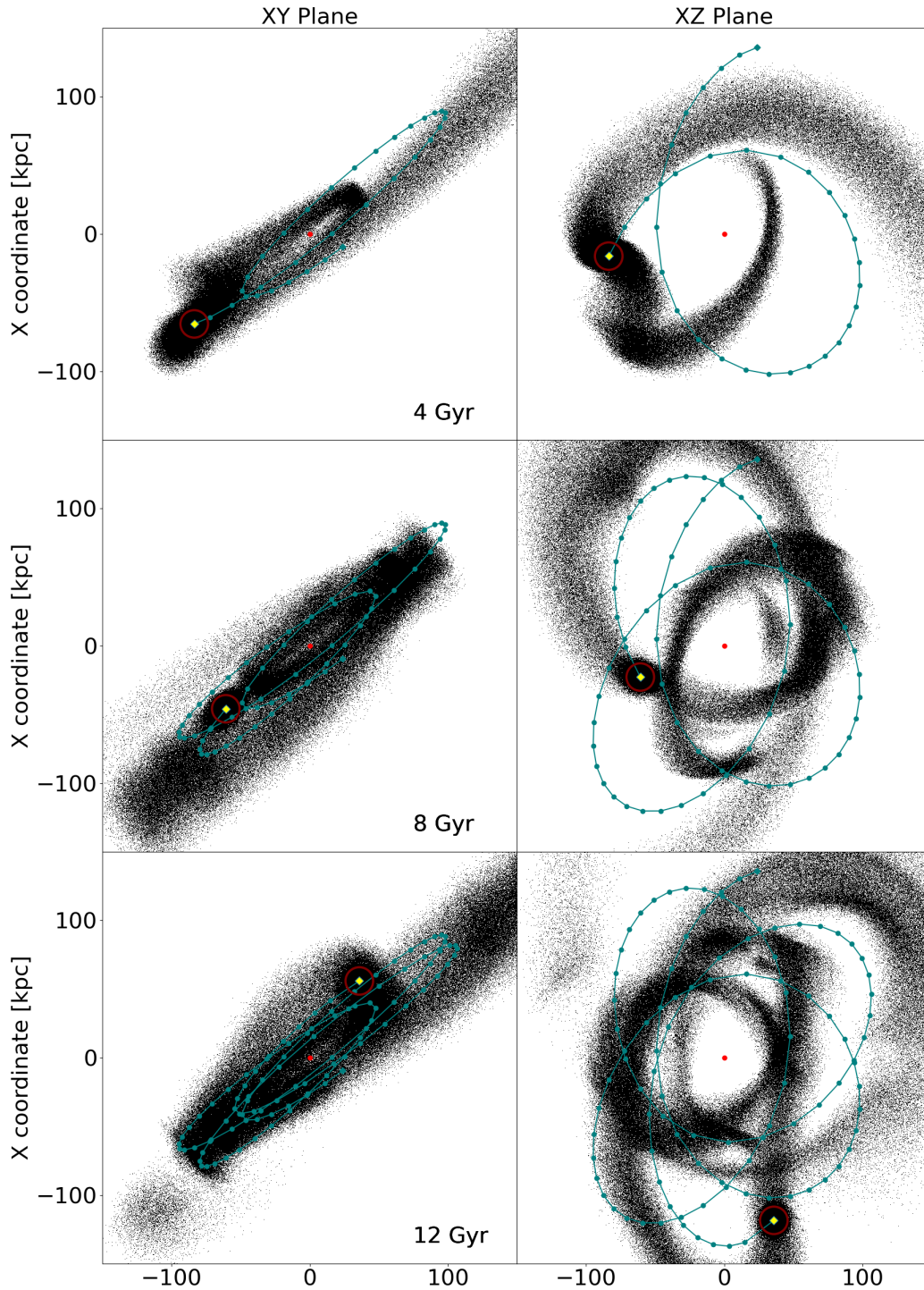
Figure 5.6: Spatial distribution of the particles of the satellite at different times in different planes in the P18-J95 simulation. Yellow diamond: current satellite center of mass position. Blue line: center of mass trajectory. Black dots: particles. Red dot: center of the system (Milky Way). Red circle: 10 kpc radius circular area centered on the center of mass as reference.

In fig 5.6 we can see how the mass loss is substantial already at 4 Gyr, two tidal tails can be identified that scatter particles on the Galactic plane. At 8 Gyr the tails have disappeared, the lost material orbits freely in the potential. In the last frame taken at 12 Gyr we observe the material scattered throughout the Galactic plane and the satellite that has been peeled down to a size comparable to the circle of radius 10 kpc shown in the figure.

More quantitative results are shown in tab 5.3, in which we report stellar and dark matter mass properties computed using $\mathcal{P}_\star(\mathcal{E})$ as in eq 4.5 with parameters given in 4.7.

	Stellar c. $[M_\odot]$	%	Dark matter c. $[M_\odot]$	%
$M_{1.6\ \mathrm{kpc}}(\mathrm{t}=0)$	$1.16 \cdot 10^7$		$3.74 \cdot 10^8$	
$M_{1.6\ \mathrm{kpc}}(\mathrm{t}=12)$	$1.09 \cdot 10^7$	(93%)	$2.64 \cdot 10^8$	(70%)
$\Delta M_{1.6\ \mathrm{kpc}}$	$0.07 \cdot 10^7$	(7%)	$1.10 \cdot 10^8$	(30%)
$M_{3.0\ \mathrm{kpc}}(\mathrm{t}=0)$	$1.28 \cdot 10^7$		$1.26 \cdot 10^9$	
$M_{3.0\ \mathrm{kpc}}(\mathrm{t}=12)$	$1.28 \cdot 10^7$	(99%)	$0.93 \cdot 10^9$	(73%)
$\Delta M_{3.0\ \mathrm{kpc}}$	$0.00 \cdot 10^7$	($< 1\%$)	$0.33 \cdot 10^9$	(27%)

Table 5.3: Stellar and dark matter loss from the satellite Fornax-like in the P18-J95 simulation.

5.3.2   NFWc model

In this section we illustrate the results obtained from the NFWc-J95 simulation for the NFWc model shown in section 3.1.

The NFWc shows a different behavior compared to the P18 Model. The density profile decreases steadily over time also in the central regions (fig 5.7(left)). ρ_{150} (right panel of fig 5.7) decrease with time and it is halved after 12 Gyr . Eventually reaching $2 \cdot 10^7$ $M_\odot/kpc^3$ as in P18-J95 simulation (see fig 5.5(right)).
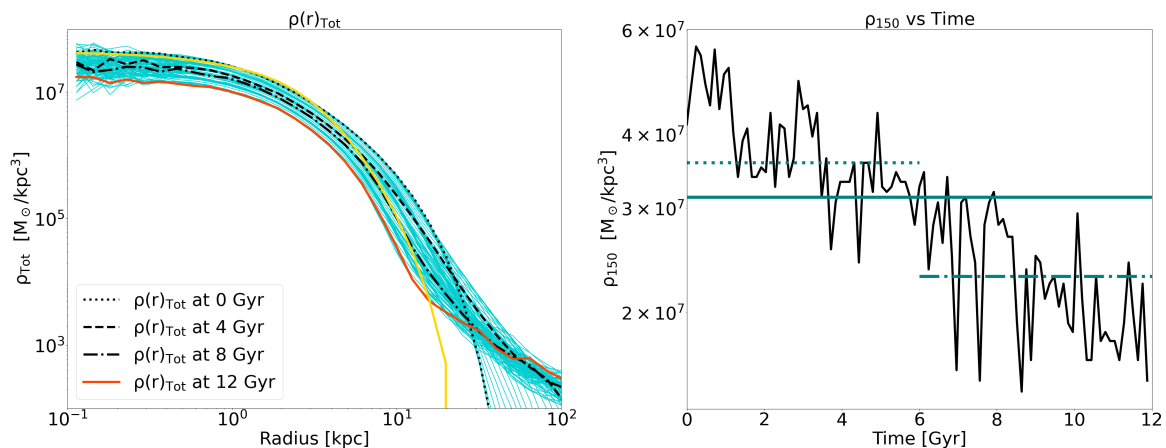

Figure 5.7: Same as fig 5.5 for the NFWc-J95 simulation.

As for the P18 model, also for the NFWc model the effect of the tidal stripping is particularly strong at $r \leq 10$ kpc. However, for the NFWc the mass loss effect is stronger, as shown by the gap between the black dashed line and the orange solid line in fig 5.7, and leads the model to a more disordered evolution than the P18 model (fig 5.8).

We recall that the NFWc has shown to be well in equilibrium if let to evolve in isolation (fig 3.6), so we can exclude artificial mass loss due to numerical effects.

Comparing the results of the P18 and the NFWc models, the P18 model looks more promising to reproduce the observed Fornax profile, if suitably modified. For this reason, we decide to set aside the NFWc model in favor of the P18 model.
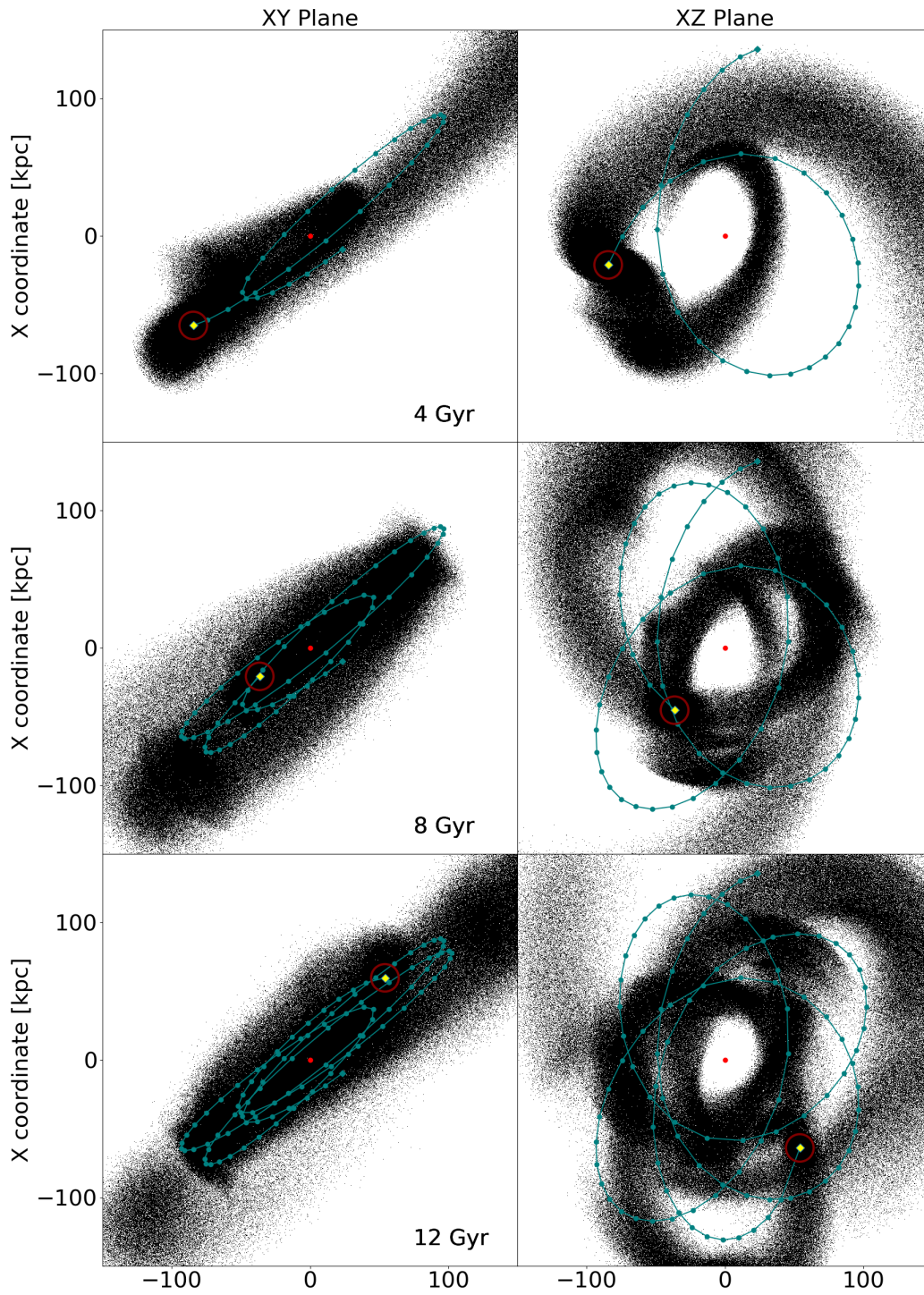
Figure 5.8: Same as figure 5.6, but for the NFWc-J95 simulation.

5.4 A modified P18 model

In this section we present a modified P18 model, which we will refer to as P18m model, created in order to obtain a Fornax-like system at the end of the simulation. It is based on the previous P18 model (presented in section 3.2), with an increase in total initial mass and density by a factor 1.4 to compensate for the expected mass loss (see fig 5.9). The properties of the P18m model are summarized in tab 5.5 with the properties of the other model presented in this thesis.
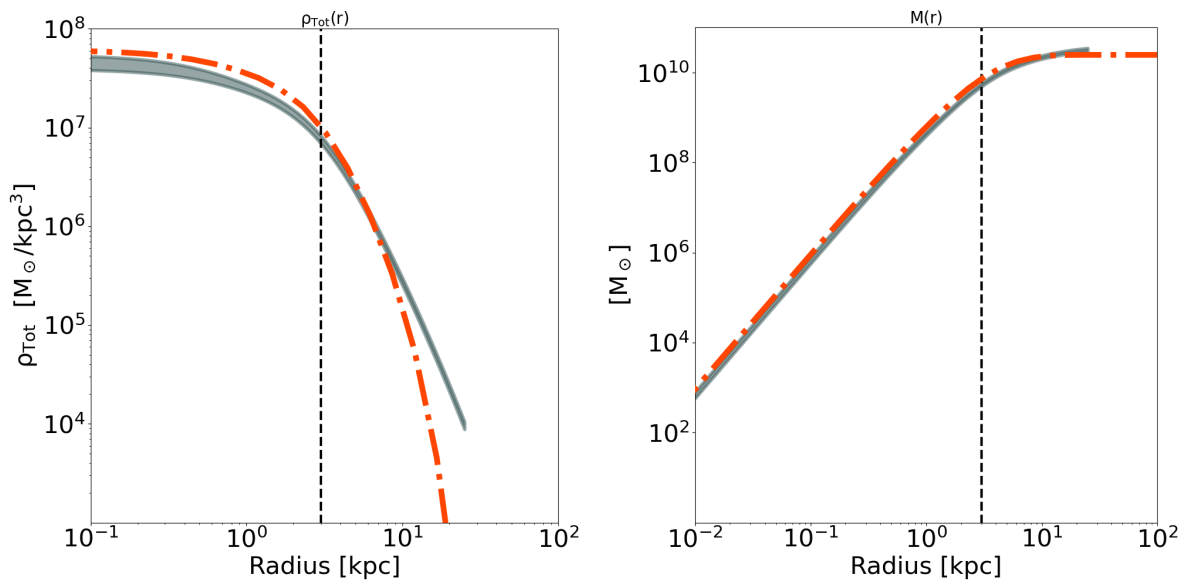

Figure 5.9: Same as fig 3.3, but for the P18m Model.

In fig 5.10 and fig 5.11, we present the results of the P18m-J95 simulation, whose parameters are in tab 5.6 and whose results will be discussed in the next section 5.5.
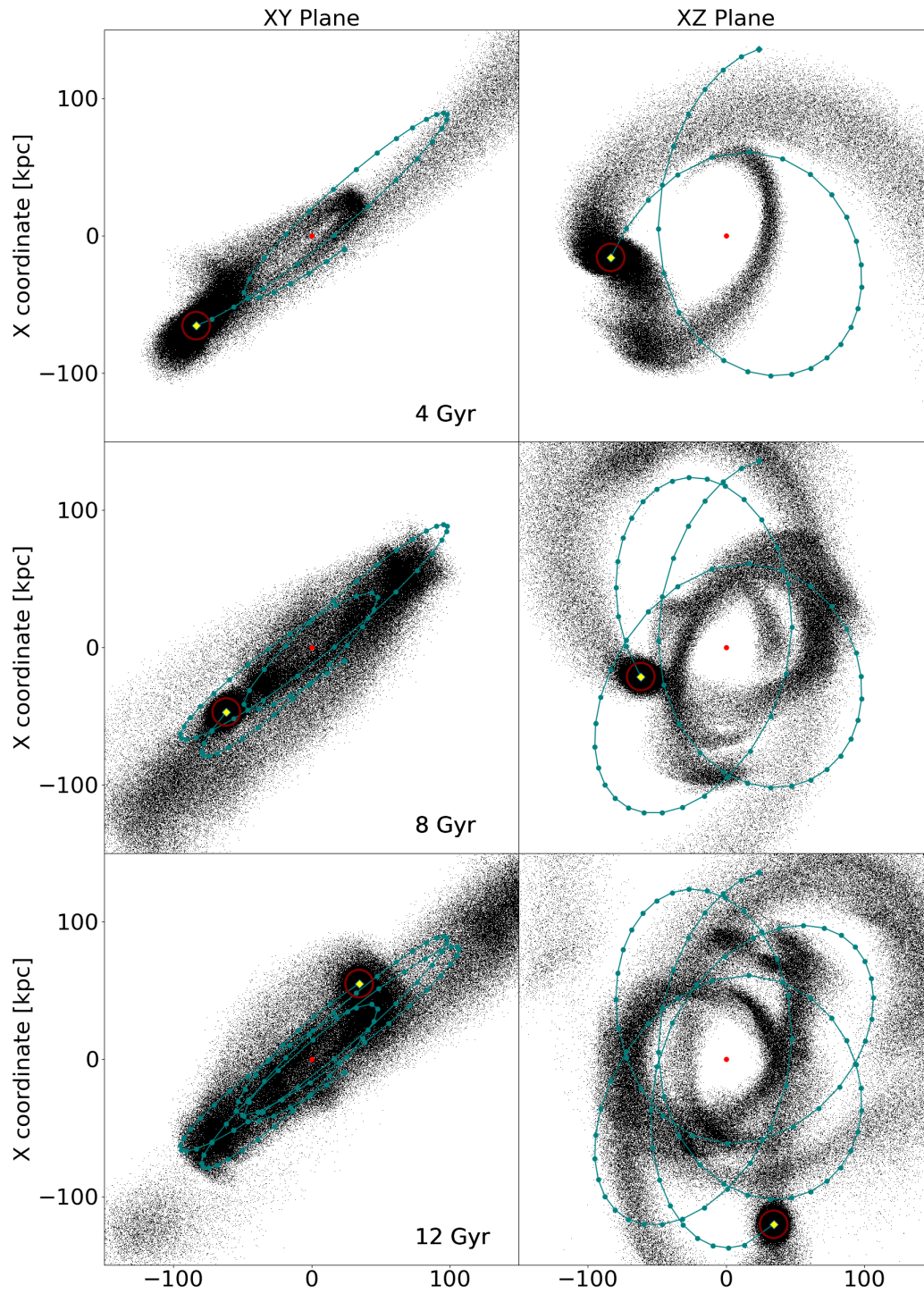
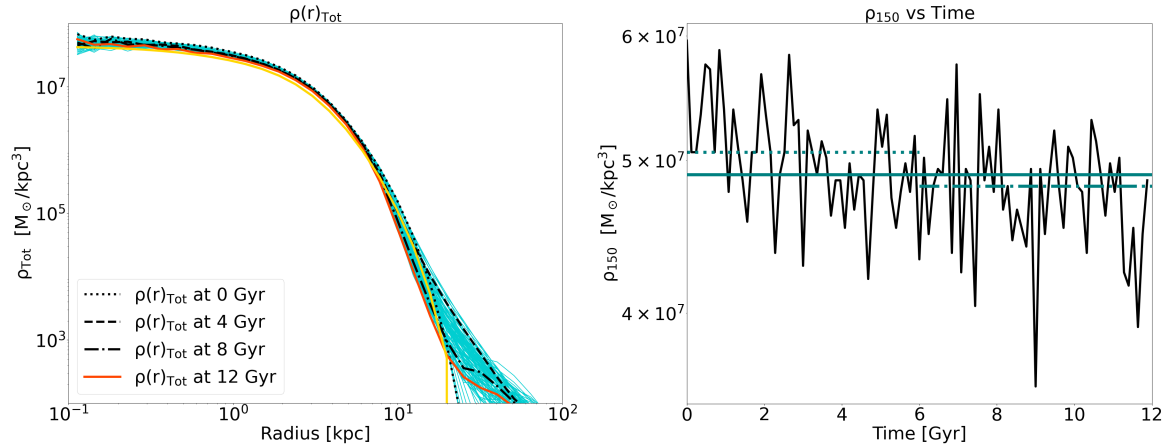Figure 5.10: Same as figure 5.6, but for the P18m-J95 simulation

Figure 5.11: Same as fig 5.5, but for the P18m-J95 simulation.

The change in mass also involves the initial energy distribution. The initial energy distribution is a combination of the kinetic and the potential gravitational energy. For this reason, the initial energy distribution curve of the P18m model (fig 5.12(left)) is different from that of the P18 model, as are the parameters of the $\mathcal{P}_\star(\mathcal{E})$ probability function (eq 4.7). The new set of parameter is:

$$A = 0.15, \qquad \alpha = 30, \qquad \beta = 0.5, \qquad \mathcal{E}_0 = 0.9. \qquad (5.4)$$

The resulting $\mathcal{P}_\star(\mathcal{E})$, stellar density and dark matter profile are shown in fig 5.12, 5.13(c)(d).
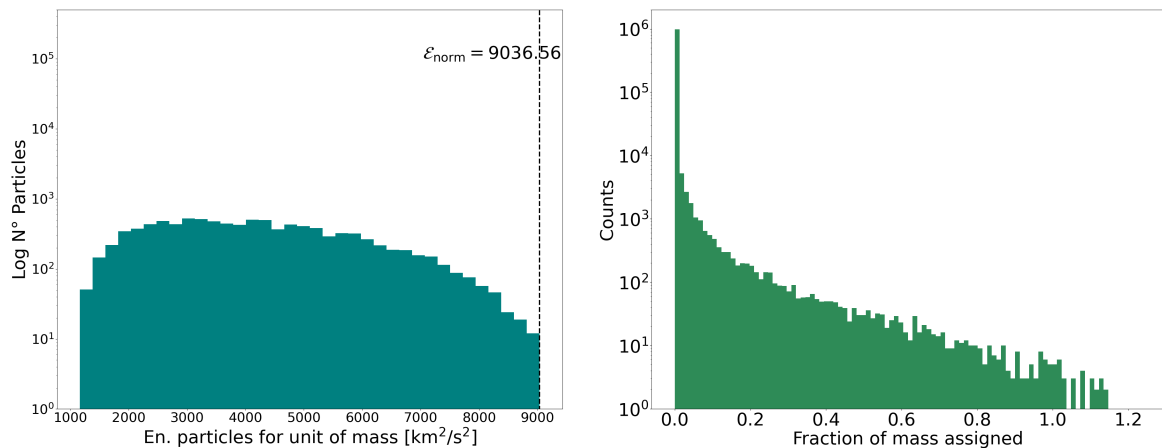

Figure 5.12: (Left) Initial energy distribution of the P18m model. (right) Initial distribution of probability of the $\mathcal{P}_\star(\mathcal{E})$ eq 5.4.
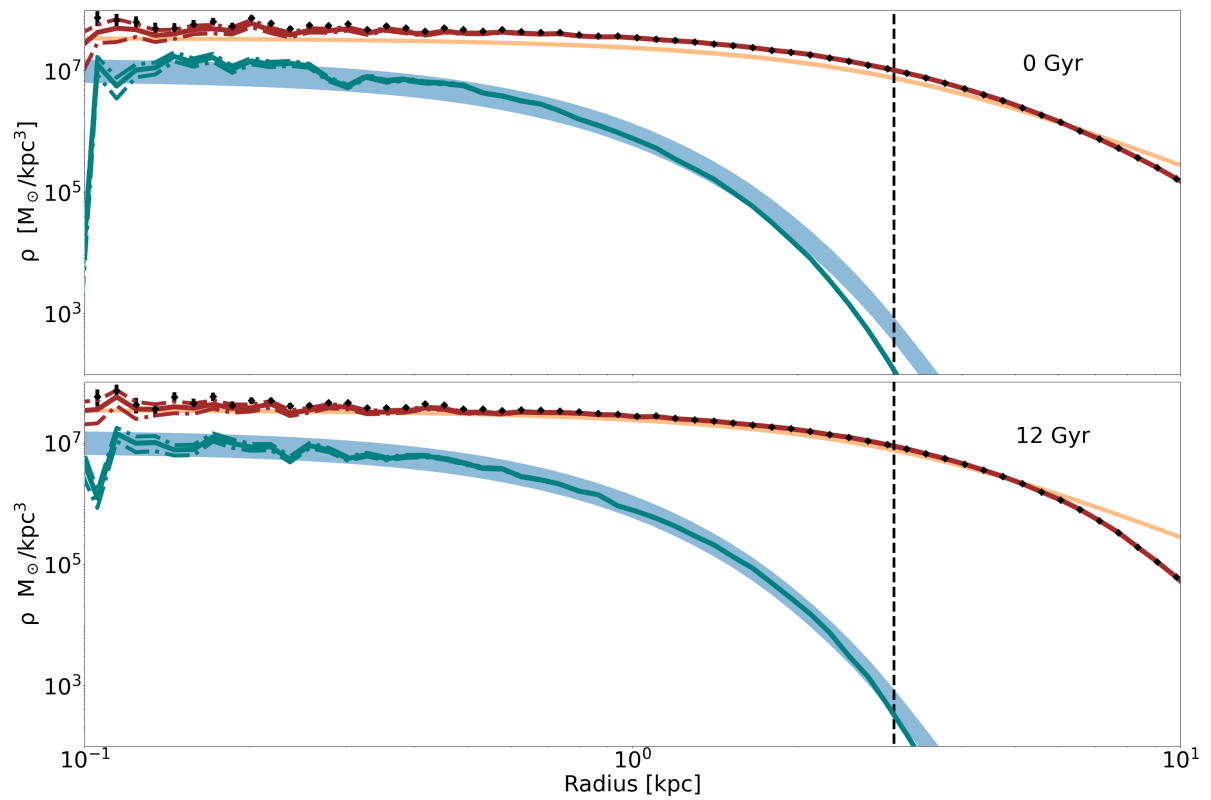
Figure 5.13: Same as fig 4.4 for the P18m-J95 simulation.

5.5   Mass loss in the P18m-J95 simulation

In this section we present the mass loss results obtained from the P18m-J95 simulation. Our goal is to determine the stellar mass loss of the Fornax-like satellite. The regions we are most interested in are the internal areas of the satellite. We want to evaluate how efficiently the stellar component is stripped away by the tidal forces caused by interactions with the Milky Way in the J95 gravitational potential.

For this reason, we choose 3 kpc and 1.6 kpc as reference radii, in order to evaluate the stellar mass variation inside the same radii used in (4). We exclude the third reference radii of 13.6 kpc chosen in (4) because we note that at radii > 10 kpc, there are essentially no more stars (see fig 5.13). The results are shown in figure 5.14 and table 5.4.
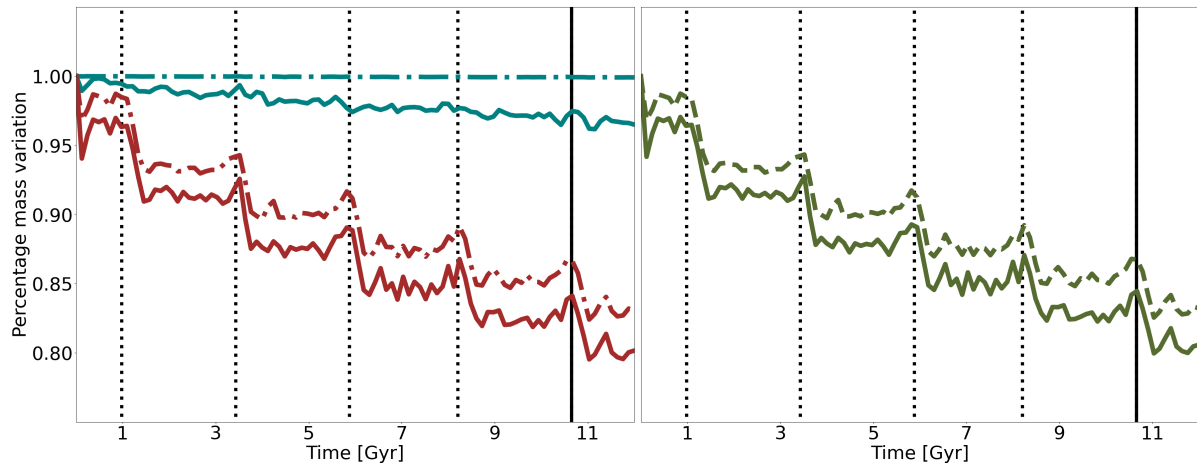
Figure 5.14: Mass loss by the satellite in 12 Gyr within a radius of 1.6 and 3 kpc for P18m-J95 simulation.
(Left panel) Red solid line: dark matter component within 1.6 kpc. Red dashed line: dark matter component within 3 kpc. Black-cyan solid line: stellar component within 1.6 kpc. Black-cyan dashed line: stellar component within 3 kpc.
(Right panel) Green solid line: dark matter + stellar component in 1.6 kpc. Green dashed line: dark matter + stellar component wihin 1.6 kpc.
(Both panel) Black dotted line: time at which the passage to the pericenter takes place. Black solid line: time at which the passage to the pericenter closest to the center takes place.

As we can see from figure 5.14, the component most affected by the tidal force, and which constitutes almost all of the lost mass, is dark matter. Instead, the stellar component seems barely touched. We could

identify a stellar flux moving outward from the inner 1.6 kpc zone, replenishing the stellar component inside the 3 kpc and allowing it to remain stable, see fig 5.14. However, the mass loss within 1.6 kpc is only 4%; in physical units the loss amounts to $5 \cdot 10^5$ M$_\odot$ versus a total stellar mass within 1.6 kpc of $1.4 \cdot 10^7$ M$_\odot$. More quantitative results are shown in tab 5.4.

For this reason, according to our result, it is therefore not likely that Fornax lost significant stellar mass through tidal interactions with the Milky Way.

Our results are very far from the 90% mass loss limit found in (22), under very different assumption. Such stellar mass loss can be obtained, according to (22), thanks to the gas expulsion from the system.

However, despite our results, the tidal mass loss scenario should not be necessary discarded. In fig 5.14 we can see that mass loss happens mainly after the passage of the pericenter. In the rest of the orbit the satellite does not lose mass, in the internal areas of the satellite the particles oscillate. For this reason, a different, more extreme, orbit with a shorter perigalactic distance or a greater number of pericenter passages could increase the stellar mass loss. Also the choice of a different Milky Way-like gravitational potential, perhaps heavier than J95 (section 5.2), since it is still not well determined, may prove useful to favour the mass loss of the Fornax dSph.

	Stellar c. [M$_\odot$]	%	Dark matter c. [M$_\odot$]	%
$M_{1.6 \text{ kpc}}(\text{t}=0)$	$1.40 \cdot 10^7$		$5.27 \cdot 10^8$	
$M_{1.6 \text{ kpc}}(\text{t}=12)$	$1.35 \cdot 10^7$	(96%)	$4.23 \cdot 10^8$	(80%)
$\Delta M_{1.6 \text{ kpc}}$	$0.05 \cdot 10^7$	(4%)	$1.04 \cdot 10^8$	(20%)
$M_{3.0 \text{ kpc}}(\text{t}=0)$	$1.47 \cdot 10^7$		$1.76 \cdot 10^9$	
$M_{3.0 \text{ kpc}}(\text{t}=12)$	$1.47 \cdot 10^7$	(99%)	$1.47 \cdot 10^9$	(83%)
$\Delta M_{3.0 \text{ kpc}}$	$0.00 \cdot 10^7$	(< 1%)	$0.29 \cdot 10^9$	(17%)

Table 5.4: Mass loss from Fornax-like satellite in the P18m-J95 simulation.

	M_{200} [M$_\odot$]	r_c [kpc]	r_s [kpc]	r_t [kpc]	$r_{\text{half mass}}$ [kpc]	t_{dyn} [Gyr]	h [$H/100$]
P18[1]	$1.44 \cdot 10^9$		3	10	4.310	$1.3 \cdot 10^{-1}$	
NFWc[2]	$4.00 \cdot 10^{10}$	1.1		15	7.727	$2.1 \cdot 10^{-1}$	0.67
P18m	$2.01 \cdot 10^{10}$		3	10	4.312	$1.1 \cdot 10^{-1}$	

Table 5.5: Summarized properties of the Fornax-like models presented in the thesis. [1] tab 3.2, [2] tab 3.1.

Simulation	I. profile	G. Potential	Orbit	Particles N°	Time [Gyr]
P18-IS[1]	P18[5]	None	None	10^6	12
NFWc-IS[1]	NFWc[6]	None	None	10^6	12
P18-J95[2]	P18[5]	J95[7]	P07ecc[8]	10^6	12
NFWc-J95[3]	NFWc[6]	J95[7]	P07ecc[8]	10^6	12
P18m-J95[4]	P18m[4]	J95[7]	P07ecc[8]	10^6	12

Table 5.6: Summarized properties of the simulations illustrated in this thesis work. [1] section 3.3, [2] subsection 5.3.1, [3] subsection 5.3.2, [4] section 5.4, [5] section 3.2, [6] section 3.1, [7] section 5.2, [8] Tab 5.1.

Chapter 6

Conclusions

In this thesis we studied with N-body simulations the stellar mass loss of the Fornax dSph, due to its tidal interaction with the Milky Way. In particular we calculated the stellar mass loss of the Fornax dSph within 3 kpc and 1.6 kpc from the center. We have selected two different Fornax-like models, one with a cored Navarro-Frank-White (NFWc hereafter) total density profile and the other with density profiles based on the numerical profile provided by Pascale et al (2018) (36).

The simulations are carried out with the collisionless code `FVFPS` (28). The Fornax-like satellite is modelled with a single component representing the total mass density distribution; with a total of 10^6 particles, whose positions and velocities have been obtained with an ergodic distribution function, i.e. dependent only on energy. The models thus obtained are expected to be at equilibrium. The two models were then let evolve in isolation for 12 Gyr. We chose 12 Gyr because it is much longer than the dynamic time of the two models. As indicators we have chosen: the $r_{\text{half mass}}$, represents the radius enclosing half mass of the satellite; the ρ_{150} is the density at 150 pc from the center; the variation of the total density profile $\rho(r)$ over time; and, as an additional indicator, with a visual proof, the conservation of spherical symmetry. With these tests we verified that numerical effects are negligible for our purpose.

We then performed simulation in which the same two models orbit in the Milky Way gravitational potential, following a Fornax-like orbit for 12 Gyr. In particular we have chosen the most eccentric orbit among those studied in Battaglia et al (2015), with a perigalactic distance of 61 kpc and an ellipticity of 0.4. At the end of the simulation we analyzed the density profiles and we decided to discard the NFWc, which is the less resilient to mass loss of the two models.

At this point we have defined the stellar component through a probability function $\mathcal{P}_\star(\mathcal{E})$, where $\mathcal{E}$ is the initial energy distribution of the particle, as the ratio between the stellar distribution function and the total distribution function. The functional form we have chosen to characterize the $\mathcal{P}_\star(\mathcal{E})$ is the generalized Schechter, whose shape and normalization are is controlled by four different parameters: α, β, A, $\mathcal{E}$. After finding a suitable set of parameters we obtained a $\mathcal{P}_\star(\mathcal{E})$ able to satisfy the constraints from (36). We built the stellar and dark matter density profiles of the simulated satellite, by weighting the particle masses using $\mathcal{P}_\star(\mathcal{E})$.

To be able to satisfy the observational constraints, at the end of the simulation, we had to compensate for the mass loss, so we run a simulation in which the initial satellite is more massive than the P18 model. From this simulation we then extracted information on the mass loss of the two components: stellar ($\sim 4\%$ within 1.6 kpc) and dark matter ($\sim 17\%$ within 3 kpc), see tab 5.4. The two results, like the behavior of the components, are similar to those found in Battaglia et al (2015) (using less flexible models). The stellar mass loss found in our simulation is insufficient to explain the *mass budget problem* (see section 1.2) ($\Delta M_{1.6 \text{ kpc}} = 0.05 \cdot 10^7 \text{ M}_\odot$), because stellar mass loss cannot significantly shift the ratio proposed in Larsen et al (2012) of $4 - 5 \cdot 10^6 \text{M}_\star$ in favor of multiple stellar population formation scenarios.

However, scenarios based on stellar mass loss from Fornax should not be considered discarded. The phenomena of mass loss can be increased, by using more extreme orbits, with smaller perigalactic distances or more pericentric passage, where, as shown in fig 5.14, the tidal force culminates and mass loss is concentrated. Furthermore, the potential of the Milky Way is not well known and in particular heavy potentials can increase the strength of tidal interactions, for given orbit. Therefore, a better exploration of possible orbits, but also of other Milky Way-like potential, could lead to different results.

Finally, we have considered the Fornax density profiles, in order to build our models and as an observational verification method and we have concentrated on the Fornax-Milky Way interactions neglecting internal process in the Fornax Globular clusters. In the future we should consider more complete models because interesting answers (22) could come from these interaction but also because the exploration of more extreme conditions will stress the Fornax system (39), possibly leading to significant stellar mass loss.

Bibliography

[1] N. C. Amorisco, A. Agnello, and N. W. Evans. The core size of the Fornax dwarf spheroidal. *Monthly Notices of the Royal Astronomical Society: Letters*, 429(1):L89–L93, 12 2012.

[2] G. Battaglia, E. Tolstoy, A. Helmi, M. J. Irwin, B. Letarte, P. Jablonka, V. Hill, K. A. Venn, M. D. Shetrone, N. Arimoto, F. Primas, A. Kaufer, P. Francois, T. Szeifert, T. Abel, and K. Sadakane. The DART imaging and CaT survey of the Fornax dwarf spheroidal galaxy. , 459(2):423–440, November 2006.

[3] Giuseppina Battaglia and Carlo Nipoti. Stellar dynamics and dark matter in Local Group dwarf galaxies. *Nature Astronomy*, 6:659–672, May 2022.

[4] Giuseppina Battaglia, Antonio Sollima, and Carlo Nipoti. The effect of tides on the Fornax dwarf spheroidal galaxy. , 454(3):2401–2415, December 2015.

[5] James Binney and Scott Tremaine. *Galactic Dynamics: Second Edition*. 2008.

[6] D. Blas. Dark matter properties from the Fornax globular cluster timing: dynamical friction and cored profiles. *arXiv e-prints*, page arXiv:2205.00289, April 2022.

[7] Jo Bovy. Dynamics and astrophysics of galaxies. https://galaxiesbook.org/index.html.

[8] Volker Bromm and Richard B. Larson. The First Stars. , 42(1):79–118, September 2004.

[9] A. Cimatti, F. Fraternali, and C. Nipoti. *Introduction to Galaxy Formation and Evolution: From Primordial Gas to Present-Day Galaxies*. 2019.

[10] David R. Cole, Walter Dehnen, Justin I. Read, and Mark I. Wilkinson. The mass distribution of the Fornax dSph: constraints from its globular cluster distribution. *Monthly Notices of the Royal Astronomical Society*, 426(1):601–613, 10 2012.

[11] Matthew G. Coleman and Jelte T. A. de Jong. A Deep Survey of the Fornax dSph. I. Star Formation History. , 685(2):933–946, October 2008.

[12] W. J. G. de Blok and A. Bosma. High-resolution rotation curves of low surface brightness galaxies. , 385:816–846, April 2002.

[13] T. J. L. de Boer, E. Tolstoy, V. Hill, A. Saha, E. W. Olszewski, M. Mateo, E. Starkenburg, G. Battaglia, and M. G. Walker. The star formation and chemical evolution history of the Fornax dwarf spheroidal galaxy. , 544:A73, August 2012.

[14] de Boer, T. J. L. and Fraser, M. Four and one more: The formation history and total mass of globular clusters in the fornax dsph. *A&A*, 590:A35, 2016.

[15] A. Dressler. Galaxy morphology in rich clusters: implications for the formation and evolution of galaxies. , 236:351–365, March 1980.

[16] Bruce G. Elmegreen. The Specific Frequency of Globular Clusters in Galaxies. , 269:469–484, December 1999.

[17] Henry C. Ferguson and Bruno Binggeli. Dwarf elliptical galaxies. , 6(1-2):67–122, November 1994.

[18] Eva K. Grebel. The local group. https://ned.ipac.caltech.edu/level5/Grebel/Grebel2.html.

[19] A. Heger and S. E. Woosley. The Nucleosynthetic Signature of Population III. , 567(1):532–543, March 2002.

[20] G. Iorio, C. Nipoti, G. Battaglia, and A. Sollima. The effect of tides on the Sculptor dwarf spheroidal galaxy. , 487(4):5692–5710, August 2019.

[21] Kathryn V. Johnston, David N. Spergel, and Lars Hernquist. The Disruption of the Sagittarius Dwarf Galaxy. , 451:598, October 1995.

[22] P. Khalaj and H. Baumgardt. Limits on the significant mass-loss scenario based on the globular clusters of the Fornax dwarf spheroidal galaxy. , 457(1):479–486, March 2016.

[23] M. Krause, C. Charbonnel, T. Decressin, G. Meynet, and N. Prantzos. Superbubble dynamics in globular cluster infancy. II. Consequences for secondary star formation in the context of self-enrichment via fast-rotating massive stars. , 552:A121, April 2013.

[24] Pavel Kroupa. On the variation of the initial mass function. , 322(2):231–246, April 2001.

[25] S. S. Larsen, J. P. Brodie, and J. Strader. Detailed abundance analysis from integrated high-dispersion spectroscopy: globular clusters in the Fornax dwarf spheroidal. , 546:A53, October 2012.

[26] S. S. Larsen, J. Strader, and J. P. Brodie. Constraints on mass loss and self-enrichment scenarios for the globular clusters of the Fornax dSph. , 544:L14, August 2012.

[27] B. Letarte, V. Hill, P. Jablonka, and E. Tolstoy. VLT/UVES Abundances of Individual Stars in the Fornax Dwarf Spheroidal Globular Clusters. In *Chemical Abundances and Mixing in Stars in the Milky Way and its Satellites*, page 268. 2006.

[28] P. Londrillo, C. Nipoti, and L. Ciotti. A parallel implementation of a new fast algorithm for N-body simulations. *Memorie della Societa Astronomica Italiana Supplementi*, 1:18, January 2003.

[29] D. Lynden-Bell. Statistical mechanics of violent relaxation in stellar systems. , 136:101, January 1967.

[30] Andrea V. Macciò, Daniel Huterer Prats, Keri L. Dixon, Tobias Buck, Stefan Waterval, Nikhil Arora, Stéphane Courteau, and Xi Kang. Creating a galaxy lacking dark matter in a dark matter-dominated universe. , 501(1):693–700, February 2021.

[31] Mario L. Mateo. Dwarf Galaxies of the Local Group. , 36:435–506, January 1998.

[32] Alan W. McConnachie. The Observed Properties of Dwarf Galaxies in and around the Local Group. , 144(1):4, July 2012.

[33] Julio F. Navarro, Vincent R. Eke, and Carlos S. Frenk. The cores of dwarf galaxy haloes. , 283(3):L72–L78, December 1996.

[34] Julio F. Navarro, Carlos S. Frenk, and Simon D. M. White. Simulations of X-ray clusters. , 275(3):720–740, August 1995.

[35] Carlo Nipoti, Giacomo Cherchi, Giuliano Iorio, and Francesco Calura. Effective N-body models of composite collisionless stellar systems. , 503(3):4221–4230, May 2021.

[36] Raffaele Pascale, Lorenzo Posti, Carlo Nipoti, and James Binney. Action-based dynamical models of dwarf spheroidal galaxies: application to Fornax. , 480(1):927–946, October 2018.

[37] Jorge Peñarrubia, Julio F. Navarro, Alan W. McConnachie, and Nicolas F. Martin. The Signature of Galactic Tides in Local Group Dwarf Spheroidals. , 698(1):222–232, June 2009.

[38] A. Renzini, F. D'Antona, S. Cassisi, I. R. King, A. P. Milone, P. Ventura, J. Anderson, L. R. Bedin, A. Bellini, T. M. Brown, G. Piotto, R. P. van der Marel, B. Barbuy, E. Dalessandro, S. Hidalgo, A. F. Marino, S. Ortolani, M. Salaris, and A. Sarajedini. The Hubble Space Telescope UV Legacy Survey of Galactic Globular Clusters - V. Constraints on formation scenarios. , 454(4):4197–4207, December 2015.

[39] Ali Rostami Shirazi, Hosein Haghi, Pouria Khalaj, Ahmad Farhani Asl, and Akram Hasani Zonoozi. The escape of globular clusters from the satellite dwarf galaxies of the Milky Way. , 513(3):3526–3540, July 2022.

[40] I. Saviane, E. V. Held, and G. Bertelli. The stellar populations of the Fornax dwarf spheroidal galaxy. , 355:56–68, March 2000.

[41] P. Schechter. An analytic expression for the luminosity function for galaxies. , 203:297–306, January 1976.

[42] Max Tegmark, Michael A. Strauss, Michael R. Blanton, Kevork Abazajian, Scott Dodelson, Havard Sandvik, Xiaomin Wang, David H. Weinberg, Idit Zehavi, Neta A. Bahcall, Fiona Hoyle, David Schlegel, Roman Scoccimarro, Michael S. Vogeley, Andreas Berlind, Tamás Budavari, Andrew Connolly, Daniel J. Eisenstein, Douglas Finkbeiner, Joshua A. Frieman, James E. Gunn, Lam Hui, Bhuvnesh

Jain, David Johnston, Stephen Kent, Huan Lin, Reiko Nakajima, Robert C. Nichol, Jeremiah P. Ostriker, Adrian Pope, Ryan Scranton, Uroš Seljak, Ravi K. Sheth, Albert Stebbins, Alexander S. Szalay, István Szapudi, Yongzhong Xu, James Annis, J. Brinkmann, Scott Burles, Francisco J. Castander, Istvan Csabai, Jon Loveday, Mamoru Doi, Masataka Fukugita, Bruce Gillespie, Greg Hennessy, David W. Hogg, Željko Ivezić, Gillian R. Knapp, Don Q. Lamb, Brian C. Lee, Robert H. Lupton, Timothy A. McKay, Peter Kunszt, Jeffrey A. Munn, Liam O'Connell, John Peoples, Jeffrey R. Pier, Michael Richmond, Constance Rockosi, Donald P. Schneider, Christopher Stoughton, Douglas L. Tucker, Daniel E. Vanden Berk, Brian Yanny, and Donald G. York. Cosmological parameters from SDSS and WMAP. *Physical Review D*, 69(10), may 2004.

[43] Athanasia Tsatsi, Andrea V. Macciò, Glenn van de Ven, and Benjamin P. Moster. A new channel for the formation of kinematically decoupled cores in early-type galaxies. *The Astrophysical Journal Letters*, 802(1):L3, mar 2015.

[44] Matthew G. Walker, Mario Mateo, Edward W. Olszewski, Oleg Y. Gnedin, Xiao Wang, Bodhisattva Sen, and Michael Woodroofe. Velocity Dispersion Profiles of Seven Dwarf Spheroidal Galaxies. , 667(1):L53–L56, September 2007.